nature communications

Article

https://doi.org/10.1038/s41467-025-68225-y

Elasto-magnetic instabilities for amplified actuation and mechanical memory

Received: 13 May 2025

Accepted: 23 December 2025

Published online: 10 January 2026

Check for updates

Seong-Yu Choi[1,7], Ji-Sung Park[2,3,7], Won Jun Song[1], Maga Kim[1], Yun Hyeok Lee[1], Yong Eun Cho[1], Hakjun Lee[1], Ho-Young Kim[2,4] ✉ & Jeong-Yun Sun[1,5,6] ✉

Instabilities can generate fast and amplified motion in mechanical systems. Here, we present an elasto-magnetic instability that combines magnetic attraction and elastic tension to create bistable dynamics. To demonstrate this, we built a coupled elasto-magnetic vibration system that produces amplified motion and greater displacement and force than a control system across a wide frequency range. We also establish design principles that can be applied to different configurations by studying the balance between magnetic and elastic forces. The system also shows inertial hysteresis, which enables mechanical memory by storing external inputs in volatile and non-volatile modes with adjustable thresholds. This dual function of amplification and memory shows how instabilities can be potentially used for programmable and adaptive soft actuation.

Mechanical systems are often constrained by their intrinsic material properties[1]. In soft materials, this manifests as low mechanical strength and slow response times[2], posing challenges for high-performance actuation. Yet, nature offers numerous examples—such as the Venus flytrap, bladderwort, and pistol shrimp—that overcome these limitations through instability-driven motion, in which elastic energy is stored and rapidly released to produce fast and powerful movements[3–7].

Inspired by such strategies, soft actuators have been engineered to incorporate structural instabilities (e.g., buckling, wrinkling, snap-through) through the use of intrinsically soft materials or compliant architectures[8–18]. These designs allow such systems to generate forces far exceeding their passive material limits. Recent developments have extended such instability-based actuation to diverse applications, including sensors[19], logic devices[20,21], and metamaterials[22–24], activated through pneumatic[12,25,26], electromagnetic[24,27,28], electrical[29,30], and chemical[13,31] stimuli.

Instability-based mechanisms inherently involve rapid, large transitions between distinct states. During these transitions, inertia—the tendency of a body to maintain its motion—is a central element of the dynamics. In structural dynamics[32,33] and in the broader literature on nonlinear phenomena[34,35], inertia governs transient responses and subsequent resettling. In soft actuation, however, it has often been treated as a passive consequence rather than an explicit design parameter. Although prior studies have shown that inertia can amplify motion[36,37], its deliberate use to drive transitions between coexisting states or to sustain motion is comparatively less explored. Harnessing both inertia and mechanical instabilities, therefore, offers a practical design strategy for soft actuators with improved adaptability and energy efficiency.

Here, we introduce an Elasto-Magnetic Instability (EsMI) that couples inertia-driven motion with tunable bistability, achieved through the interplay between magnetic attraction and elastic tension. To realize this mechanism, we developed a Coupled Elasto-Magnetic Vibration (C-EsMV) system that integrates permanent magnets and an elastic membrane, forming a bistable architecture capable of enhancing kinetic energy conversion by over three orders of magnitude compared to a non-coupled control system (NC-EsMV) (Fig. 1a, b). This design quantifies and leverages the balance between characteristic magnetic

[1]Department of Materials Science and Engineering, Seoul National University, Seoul, Republic of Korea. [2]Department of Mechanical Engineering, Seoul National University, Seoul, Republic of Korea. [3]Institute of Mechanical Engineering, École Polytechnique Fédérale de Lausanne, Lausanne, Switzerland. [4]Institute of Advanced Machines and Design, Seoul National University, Seoul, Republic of Korea. [5]Research Institute of Advanced Materials (RIAM), Seoul National University, Seoul, Republic of Korea. [6]SNU Energy Initiative, Seoul National University, Seoul, Republic of Korea. [7]These authors contributed equally: Seong-Yu Choi, Ji-Sung Park. ✉e-mail: hyk@snu.ac.kr; jysun@snu.ac.kr

https://doi.org/10.1038/s41467-025-68225-y

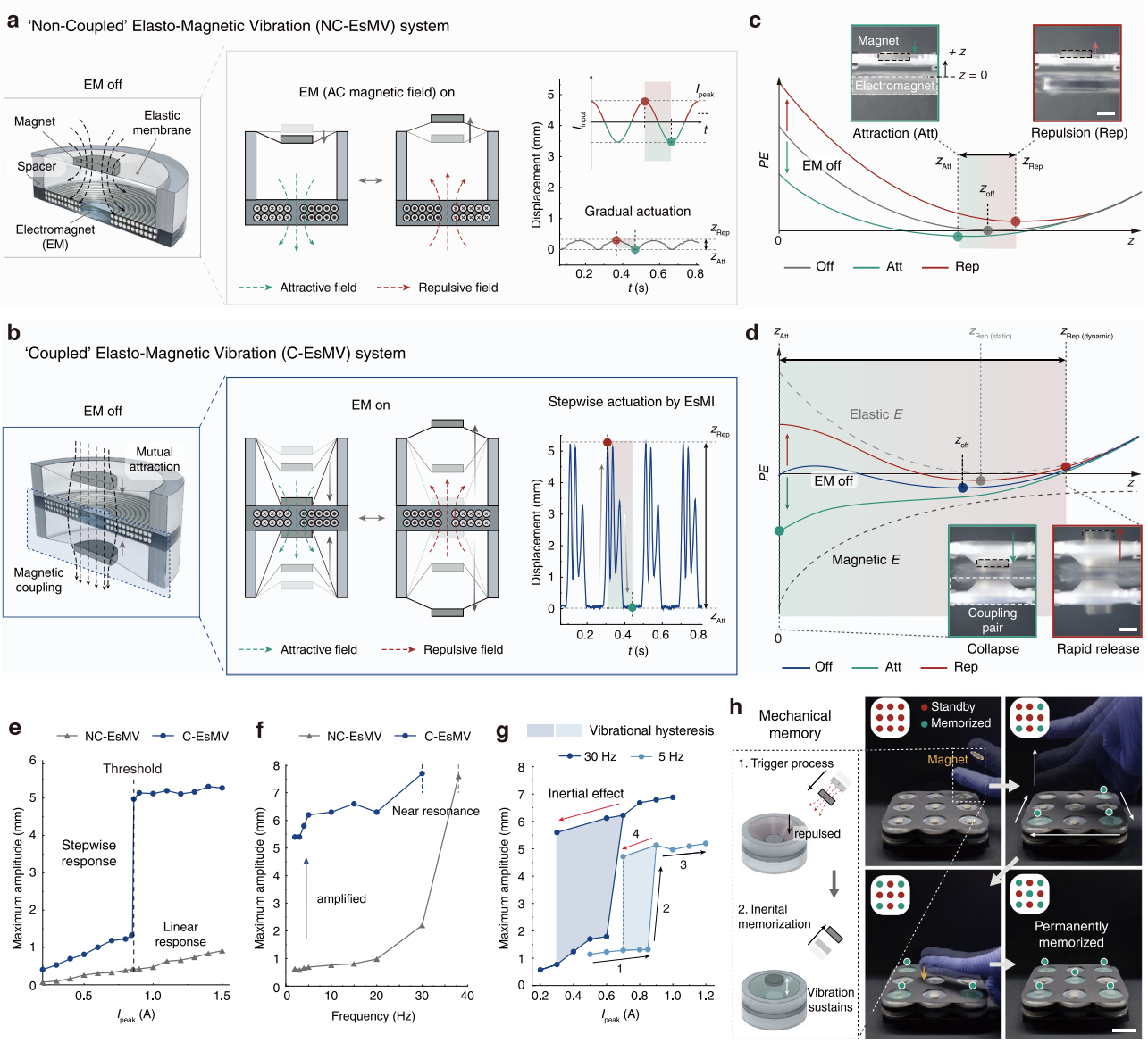

Fig. 1 | Coupled elasto-magnetic vibration (C-EsMV) system enabling amplified actuation and mechanical memory. a, **b** Configurations of elasto-magnetic vibration (EsMV) systems: **a** non-coupled (NC-EsMV) and **b** coupled (C-EsMV). When an AC is applied to an electromagnet, permanent magnets vibrate due to cycles of attractive (green dashed arrow) and repulsive (red dashed arrow) field. Even with the same input current, the two systems exhibit entirely different vibration behaviors (f_i = 5 Hz, I_{peak} = 0.86 A, Scale bar: 3 mm). **c**, **d** Schematic representations of potential energy landscapes for **c** NC-EsMV and **d** C-EsMV. Under alternating magnetic fields (attractive/ repulsive) applied by an electromagnet, the potential energy oscillates from each system's equilibrium state (z_{off}), driving vibrations. In C-EsMV, the elastic potential energy of the membrane (gray dashed line) and the magnetic attraction between coupled magnets (black dashed line) combine to create Elasto-magnetic instability. The large inertia in C-EsMV allows the magnet to overshoot the static equilibrium position, extending from $z_{Rep,\ (static)}$ to $z_{Rep,\ (dynamic)}$, resulting in vibration amplitudes significantly larger than NC-EsMV. **e**–**g** Key features of the C-EsMV system: **e** Maximum vibration amplitude as a function of input current, showing a nonlinear, stepwise response in C-EsMV compared to the linear response in NC-EsMV (f_i = 5 Hz). **f** Vibration amplitude across frequencies, with C-EsMV maintaining large amplitudes from low frequencies to near resonance (I_{peak} = 1 A). **g** Vibrational hysteresis by inertia, where amplified vibration persists below the current threshold. This effect is more pronounced near resonance (f_i = 30 Hz) due to increased energy absorption. **h** Non-contact, non-volatile mechanical memory arrays. When a magnetic trigger is applied to each cell, it transitions from the *standby* to the *memorized* state, permanently recording the external mechanical trigger (f_i = 30 Hz, Scale bar: 2 cm).

(F^*_{MM}) and elastic (F^*_{ES}) forces, establishing a scalable framework for inertia-enhanced actuation. Incorporating an electromagnet further enables real-time modulation of the instability landscape, leading to reconfigurable transitions and nonlinear, stepwise amplification with vibration-induced hysteresis. This hysteretic behavior enables mechanical memory, allowing external triggers to be encoded into volatile and non-volatile modes with tunable activation thresholds.

Results

Elasto-magnetic instability (EsMI)

When two magnets with identical polar orientations approach each other, their attractive force rises sharply, leading to the collapse-like motion of magnets (Supplementary Fig. 1a). They accelerate toward each other and adhere, settling into the lowest-energy configuration. Although this magnetic coupling has the potential to utilize the inherent strength of magnets, due to its accelerating nature when attracted, it has been mainly used in applications such as array[38], field alignment[39], and structure reconfiguration[40,41]. To harness the powerful magnetic

motion, we adopt an elastic membrane acting as a spring, capable of storing and releasing energy (Supplementary Fig. 1b). The resulting combination of magnetic and elastic force generates an elasto-magnetic instability (EsMI) with two stable states (Fig. 1d, blue line).

Elasto-magnetic vibration (EsMV) systems

To validate the instability arising from magnetic collapse, two types of elasto-magnetic vibration systems were developed: one consists of a single elastic membrane-magnet composite positioned above one side of the electromagnet, with acrylic spacers to adjust the gap (NC-EsMV, Fig. 1a). The other employs two membrane-magnet composites on either side of the electromagnet, coupled through mutual attraction (C-EsMV, Fig. 1b). The electromagnet, driven by a sinusoidal input alternating current (AC) signal, generates a magnetic field that cyclically attracts and repels the magnet(s), inducing oscillatory motion (Supplementary Fig. 2). This motion stretches the membrane, producing an elastic counterforce.

To analyze the basic behaviors of both systems, we calculated the elasto-magnetic potential energy and the corresponding equilibrium positions as a function of input current. As shown in Supplementary Fig. 3, the NC-EsMV system remains monostable over the entire current range (−2.0 A to +2.0 A), and the equilibrium position changes only slightly with current ($\Delta z/D \approx 0.25$). In contrast, the C-EsMV system exhibits bifurcation in behavior, so that the energy landscape alternates between monostable and bistable regimes as the current varies, leading to a much larger shift in equilibrium position ($\Delta z/D > 1$). The appearance of a bistable regime indicates the presence of an elasto-magnetic instability (EsMI), arising from the magnetic attraction between the paired magnets and the elastic restoring force of the membranes. This distinction is directly reflected in the vibration behavior. In NC-EsMV, the magnets' natural collapse motion is not utilized; the system relies solely on the electromagnet to drive magnet's movement, resulting in only small-amplitude vibrations between z_{Att} and z_{Rep} (Fig. 1a). This behavior is consistent with the potential energy graph, where the magnet's equilibrium position, determined by the minimum of the potential energy, changes only slightly along the z-axis during each cycle of electromagnetic attraction and repulsion (Fig. 1c).

In C-EsMV, however, the system inherently exhibits a strong magnetic attraction between the magnet-membrane composites even without an applied electromagnetic field (i.e., EM field off, $z = z_{off}$), resulting in an energy barrier within the potential energy landscape. When an attractive electromagnetic field is applied, the magnets are drawn closer until reaching a critical distance, at which point they collapse onto the electromagnet surface, storing potential energy in the membrane ($z = z_{Att}$). Upon switching to a repulsive field, the equilibrium shifts from z_{Att} to $z_{Rep,\,(static)}$, where the stored energy is rapidly converted into kinetic energy, yielding significantly larger vibrations compared to NC-EsMV (Fig. 1b and d and Supplementary Video 1). In addition, the composite's initially high inertia further amplifies the vibration amplitude, extending the peak position from $z_{Rep,\,(static)}$ to a dynamically overshoot position $z_{Rep,\,(dynamic)}$.

A noteworthy characteristic of C-EsMV is its nonlinear, stepwise response to input signals (Fig. 1e). For example, when $I_{peak} \leq 0.85$ A, both systems exhibit small-amplitude vibrations. However, a slight increase to 0.86 A causes C-EsMV to transition to high amplitude vibrations, while NC-EsMV remains nearly unchanged. Achieving large outputs with small input changes is crucial for system efficiency, and this threshold value can be readily tuned through structural design adjustments.

Resonance effect and hysteric behavior

Elasto-magnetic vibrations, driven by the electromagnet's signal, are governed by both the membrane's natural frequency and the external signal frequency. In NC-EsMV, vibrations intensify near resonance due to increased energy absorption but remain confined to a narrow frequency range (Fig. 1f). In contrast, C-EsMV—enabled by the EsMI—sustains large-amplitude vibrations over a broader frequency range, including low frequencies in particular, thereby enhancing versatility. At resonance, the input energy is accumulated coherently with the oscillation, whereas beyond resonance, phase mismatch suppresses energy coupling, leading to the eventual decay observed experimentally (detailed in Supplementary Note 3).

Another distinctive feature of C-EsMV is its vibrational hysteresis (Fig. 1g and Supplementary Video 2). Once triggered, the system retains amplified motion even as the input current falls below the critical threshold for amplification, exhibiting behavior analogous to a Schmitt trigger[25] under both low- and relatively high-frequency conditions (f_i = 5 Hz and 30 Hz). This retention originates from the inertia of the magnets, which sustains continuous exchange between elastic and kinetic energy once amplification is initiated. The system maintains stable vibration amplitudes over 60,000 cycles (Supplementary Fig. 4), demonstrating its ability to preserve performance under reduced energy input. Near resonance (~ 30 Hz), this hysteretic effect becomes more pronounced, highlighting the roles of acceleration and inertia in maintaining dynamic stability.

This inertia-driven mechanism allows us to build a mechanical memory, which "memorizes" external triggers as amplified vibrations without additional electrical input. As illustrated in Fig. 1h, a magnet attached to a finger repels the magnet on the membrane, leading to the storage of additional elastic potential energy. Once the finger is removed, the system keeps vibrating. This non-contact magnetic trigger shifts the system from a *standby* state (weakened vibration) to a *memorized* state (amplified vibration). The *memorized* state remains stable indefinitely unless the electromagnet is off or the system is intentionally reset (Supplementary Video 3). Further details of this behavior are discussed in Fig. 5, focusing on the application of mechanical memory.

Mechanism of EsMV systems

To elucidate the magnetic coupling effects in the EsMV system, we analyzed the forces and energy exchanges during actuation using an analytical model detailed in Supplementary Notes 1 and 2.

We tracked the time evolution of magnets' position to capture acceleration and the consequent inertial effects. In Fig. 2, potential energy (blue line) and kinetic energy (red line) were plotted over time, with the magnet's position marked by yellow circles at characteristic moments. In the NC-EsMV system (Fig. 2a, b), the magnet's position (z) is measured from the electromagnet surface and the equilibrium position at the off-state corresponds to the initial position D ($z_{off} = D$). During the repulsive phase (Fig. 2a), total potential energy increases ($t_0 \leq t \leq t_2$), displacing the magnet in the positive z-direction with minimal kinetic energy (~10^{-4} mJ). During the attractive phase (Fig. 2b), the potential energy decreases ($t_2 \leq t \leq t_4$), pulling the magnet back with a negligible overshoot (~ 0.2 mm) owing to low inertia, as indicated by the shaded area.

In contrast, in the C-EsMV system (Fig. 2c, d), the mutual attraction between the magnets draws them slightly closer at the off-state ($z_{off} < D$). When magnetic and elastic energies are appropriately balanced, they create an energy barrier between the upper ($z = z_{off}$) and lower equilibrium ($z = 0$) points. This barrier allows energy accumulation until a critical threshold is reached, resulting in time-varying "snap-through" behavior. During the repulsive phase ($t'_0 \leq t < t'_2$), the magnets remain at the bottom surface (Fig. 2c) until the electromagnetic field dissipates the barrier. Once the barrier is removed, the stored elastic energy accelerates the magnet ($t'_2 \leq t \leq t'_3$), causing it to overshoot the upper static equilibrium by ~3 mm due to significant inertia. During the attractive phase ($t'_4 \leq t \leq t'_6$), the magnet returns to $z = 0$, completing the cycle (Fig. 2d).

https://doi.org/10.1038/s41467-025-68225-y

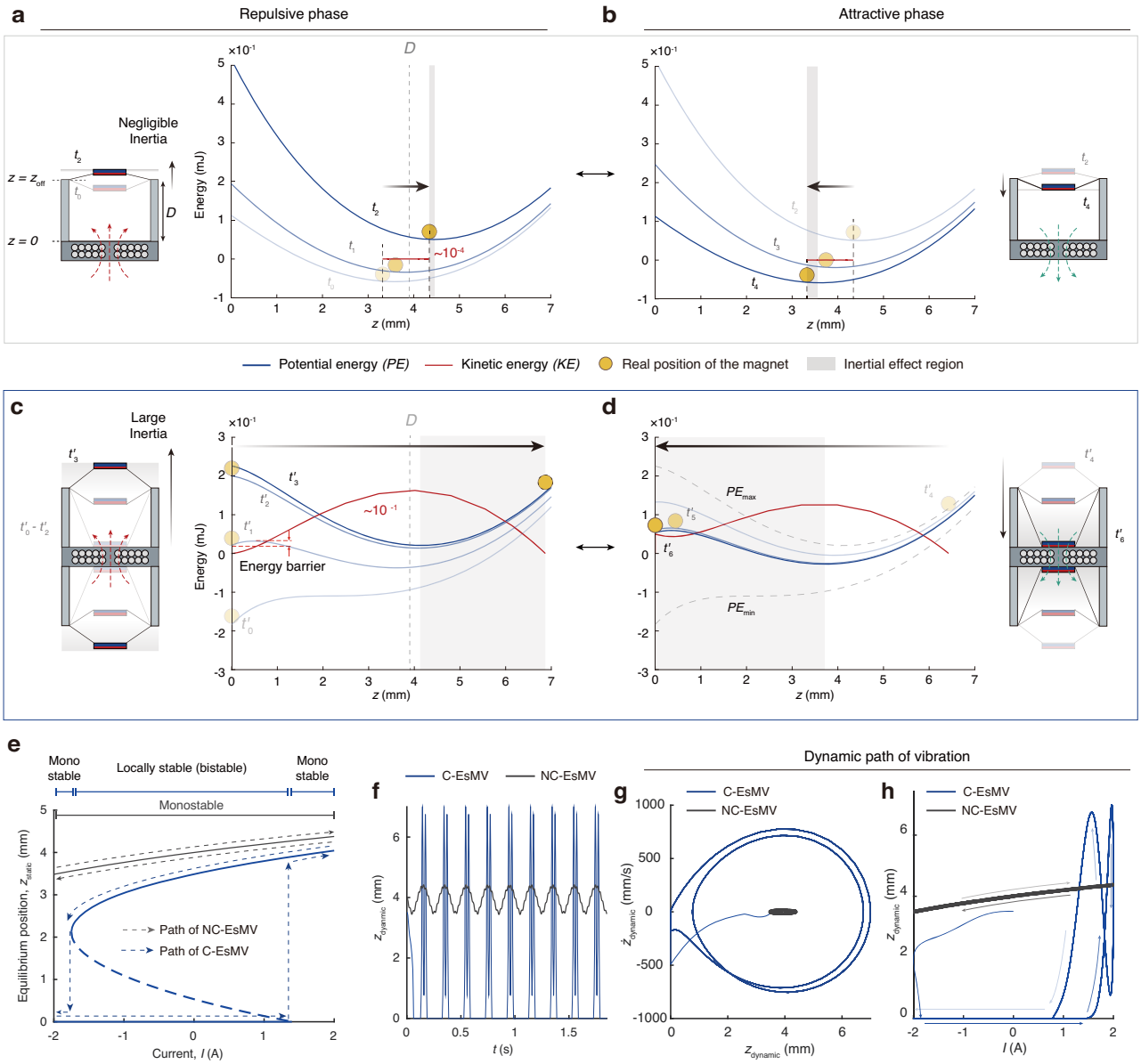

Fig. 2 | Mechanism of an amplification in EsMV systems. a, **b** Energy diagrams of NC-EsMV during the **a** repulsive phase (t_0–t_2) and **b** attractive phase (t_2–t_4). Kinetic energy (red) and potential energy (blue) are plotted over time. The yellow ball indicates the magnet's actual position, considering its inertia. In NC-EsMV, the magnet oscillates around static equilibrium points ($z = z_{off}$) with low kinetic energy (~10^{-4} mJ). **c**, **d** Energy diagrams of C-EsMV during the **c** repulsive phase (t'_0–t'_3) and **d** attractive phase (t'_4–t'_6). When this barrier is overcome by the combined effects of elastic restoration force and electromagnetic repulsion, the magnet is launched with significantly higher kinetic energy (~10^{-1} mJ), resembling a slingshot motion (t'_2–t'_3). **e**–**h** Static and dynamic vibration analyses of NC-EsMV and C-EsMV systems. **e** Motion trajectories of each system derived from bifurcation diagram analysis. **f** Time-dependent vibration amplitudes showing dynamic responses of each system. **g** Phase portraits illustrating distinct dynamic states. **h** Dynamic vibration trajectories under sinusoidal input. All analysis was conducted representatively at $f_i = 5$ Hz and $I_{peak} = 2.0$ A.

Throughout a cycle, NC-EsMV exhibit small oscillations with net force and kinetic energy remaining low. The low net force and kinetic energy stem from inefficient energy transfer, as most of the electromagnet-generated potential energy dissipates into the surrounding air rather than converting effectively into kinetic energy. Consequently, the NC-EsMV system results in limited energy exchange and subdued motion. In contrast, the C-EsMV system establishes a critical threshold that enables efficient conversion of electrical input into mechanical motion. This configuration enables improved conversion efficiency through elasto–magnetic coupling, allowing a larger portion of the supplied power to be stored and released as kinetic energy. This efficient energy transfer yields kinetic energy levels approximately 1000 times greater than those in the NC-EsMV system (Supplementary Fig. 5). Based on the above energy landscape analysis, we further examined the equilibrium transition paths of both systems. In the NC-EsMV, the vibration follows a single monostable branch, with small positional shifts corresponding to minor equilibrium changes as the current varies between attractive and repulsive phases. In contrast, the C-EsMV exhibits bifurcation in behavior: under increasing attractive current, the magnet moves along the upper stable branch until the potential barrier diminishes and upper state loses stability, leading to an abrupt transition to the lower branch (collapse), as the current reverses, it jumps back—forming a complete hysteretic cycle (Fig. 2e). When dynamic effects are taken into account, however, the actual displacement ($z_{dynamic}$) becomes significantly larger than the static equilibrium shift, as shown in Fig. 2f. The corresponding phase portrait

confirms that C-EsMV reaches a much higher velocity and converges to a large-amplitude limit cycle compared with NC-EsMV (Fig. 2g). Finally, Fig. 2h illustrates the real-time vibration trajectory under a sinusoidal input, visualizing a single current sweep and the resulting path-dependent oscillation.

Design principles of C-EsMV system

Our proposed mechanism offers versatility in design, relying on the balance of two dominant forces, magnetic attraction and elastic tension, emphasizing the importance of choosing suitable characteristic forces. The vibrational displacement is indeed influenced by the size of the magnets and the stiffness of the elastic membrane. However, these parameters were systematically incorporated into both our experimental design and simulations to ensure consistent scaling behavior.

To guide system design, we define characteristic scales of each force. For the characteristic elastic force (F^*_{ES}), we account for both magnet and membrane dimensions:

$$F^*_{ES} = \frac{\pi E}{2(1+\nu)} h_m \lambda_p^2 \left(R_m + R_a\right), \tag{1}$$

where E, ν, h_m, R_m, λ_p are Young's modulus, Poisson's ratio, pre-stretched membrane thickness, membrane radius, and the prestretch ratio of the membrane, respectively. R_a is the radius of the attached magnet. The characteristic magnetic force, F^*_{MM}, is defined as the maximum attractive force when the magnets are collapsed ($z = 0$):

$$F^*_{MM} = \frac{\mu_0}{2} M_a M_b \Omega|_{z=0}, \tag{2}$$

where μ_0 is the vacuum permeability, M_a and M_b are the magnetizations, and $\Omega|_{z=0}$ is a geometric factor determined by the magnet geometry. The full derivation and structural parameters are provided in Supplementary Fig. 6 and Supplementary Note 1.

By adjusting magnet thickness (h_a and h_b) and using elastic membranes with varying moduli (E) while maintaining constant magnetization (M), we developed a design map for the maximum vibration amplitude resulting from those elastic and magnetic forces at each optimal initial position (D_{opt}, Fig. 3a, top). We also defined three actuation states: *collapsed* (magnetic force dominates, preventing the membrane from detaching the magnets touching the electromagnet), *weakened* (elastic force dominates, preventing magnets from retouching the electromagnet), and *amplified* (balanced forces allow both detachment and reattachment of magnet to electromagnet for large amplitude vibrations) (Fig. 3a, bottom). The maximum amplitude is attained along the white dashed line in Fig. 3a, where $F^*_{MM} \approx F^*_{ES}$, establishing optimal conditions for amplified vibration. Supplementary Note 4 and Supplementary Fig. 7 present additional design maps illustrating the conditions for amplification capabilities, amplifiable range ($\Delta D = D_{max} - D_{min}$), optimal initial position (D_{opt}), and maximum velocity (v), acceleration (a), and kinetic energy (KE).

To validate this design map, we experimentally examined three cases with distinct force profiles as shown in Fig. 3b–d with Supplementary Table 2: *Cases I* and *II* share the same elastic force but differ in magnetic force, while *Cases II* and *III* have the same magnetic force but different elastic forces. System states (*collapsed, weakened*, or *amplified*) depend on peak current (I_{peak}) and initial position (D) (Fig. 3b–d).

In *Case I* ($F^*_{ES} = 0.2419$ N, $F^*_{MM} = 0.0348$ N), weak magnetic force enables amplified vibrations (green triangles) only at short distances (D) or high currents. Otherwise, the system remains in the *weakened* state (blue circles) (Fig. 3b). In *Case II* ($F^*_{ES} = 0.2419$ N, $F^*_{MM} = 0.2072$ N), the magnets collapse (red dots) when D is small, but achieve amplified vibrations at larger D (Fig. 3c). *Case III*, with increased elastic force ($F^*_{ES} = 0.6289$ N, $F^*_{MM} = 0.2072$ N), exhibits amplified vibrations at small D or high currents. However, at larger D, the system falls into a weakened state without amplification (Fig. 3d). Since *Case II* leverages the most significant elastic potential, it is identified as the most desirable configuration.

To quantitatively compare these three cases, we evaluated the maximum amplitude and kinetic energy at each optimal point α, β, and γ under the same input current ($I_{peak} = 1.5$ A). At point α (*Case I*, $D = 2.5$ mm), weak attraction keeps the magnets in a *weakened* state, despite being closest to the electromagnet. At points β (*Case II*, $D = 4.0$ mm) and γ (*Case III*, $D = 3.0$ mm), amplified vibration occurs in both cases at the boundary between *amplified* and *weakened* states, but *Case II* exhibits the highest performance, as experimentally measured in Fig. 3e.

To further assess the performance of *Case II*, we analyzed the ratio of energy conversion efficiencies ($\varepsilon_{C/NC}$, the ratio of the maximum kinetic energy of C-EsMV to that of NC-EsMV under identical electrical input) as a function of I_{peak} with $D = 4.0$ mm. This ratio peaks immediately after amplification begins, reaching as high as 700, then gradually declines (Fig. 3c and f). This enables efficient, thermally stable operation of C-EsMV over time (Supplementary Fig. 8).

Conversely, by fixing I_{peak} at 2.0 A and varying the distance D, we observed sequential transitions in system behavior (Fig. 3c and g and Supplementary Video 4). As the magnet-membrane composite approaches the electromagnet, the system moves from the *weakened* state to the *amplified* state, and finally to a *collapsed* state. In contrast, non-coupled systems display only monotonic changes in amplitude.

We further explored the system's behavior across varying initial position (D) and combinations of elastic and magnetic forces (see Supplementary Note 5 and Supplementary Figs. 9–11).

In particular, *weakened* states are classified into *shootable* and *non-shootable* regimes based on whether the actuator can transition into amplified state upon external triggering (Supplementary Fig. 9e, f). This triggering process, which we term "shooting," refers to a momentary stimulus that propels the magnet across the energy barrier separating the coexisting states (*weakened* and *amplified*). As shown in Supplementary Fig. 12, when the input current was increased above the onset threshold ($I_{th,\ on}$) and then reduced (shooting), the system exhibited a sudden transition from a weakened to an amplified vibration state, maintaining the large amplitude even after the current returned to the initial current level ($I_{peak} \approx 1.3$ A). In contrast, systems that never exceeded $I_{th,\ on}$ (non-shooting), remained confined to low-amplitude oscillations because the available energy was insufficient to overcome the potential barrier (i.e., the basin boundary between the two attractors). Experimentally, a brief electrical trigger induced this dynamic shift, confirming that the vibration state could be switched and retained through a transient perturbation.

This behavior was further validated through simulation (Supplementary Fig. 13). In the model, a short high-current pulse ($I_{peak} = 2.0$ A) served as the electrical trigger, driving the system across the potential barrier. Comparing the bifurcation diagrams before and after shooting at $I_{peak} = 1.4$ A revealed that the response followed a distinct path along the upper stable branch, resulting in a larger limit-cycle oscillation even in the absence of resonance. The persistence of this amplified vibration after returning to the lower input current arises from inertia, which provides residual kinetic energy to sustain oscillations around the new equilibrium branch. This inertia-driven retention is stably maintained and was further validated as an efficient energy conversion mechanism (Supplementary Fig. 14). It constitutes the vibrational hysteresis–based mechanical memory, which is further analyzed in Fig. 5.

https://doi.org/10.1038/s41467-025-68225-y

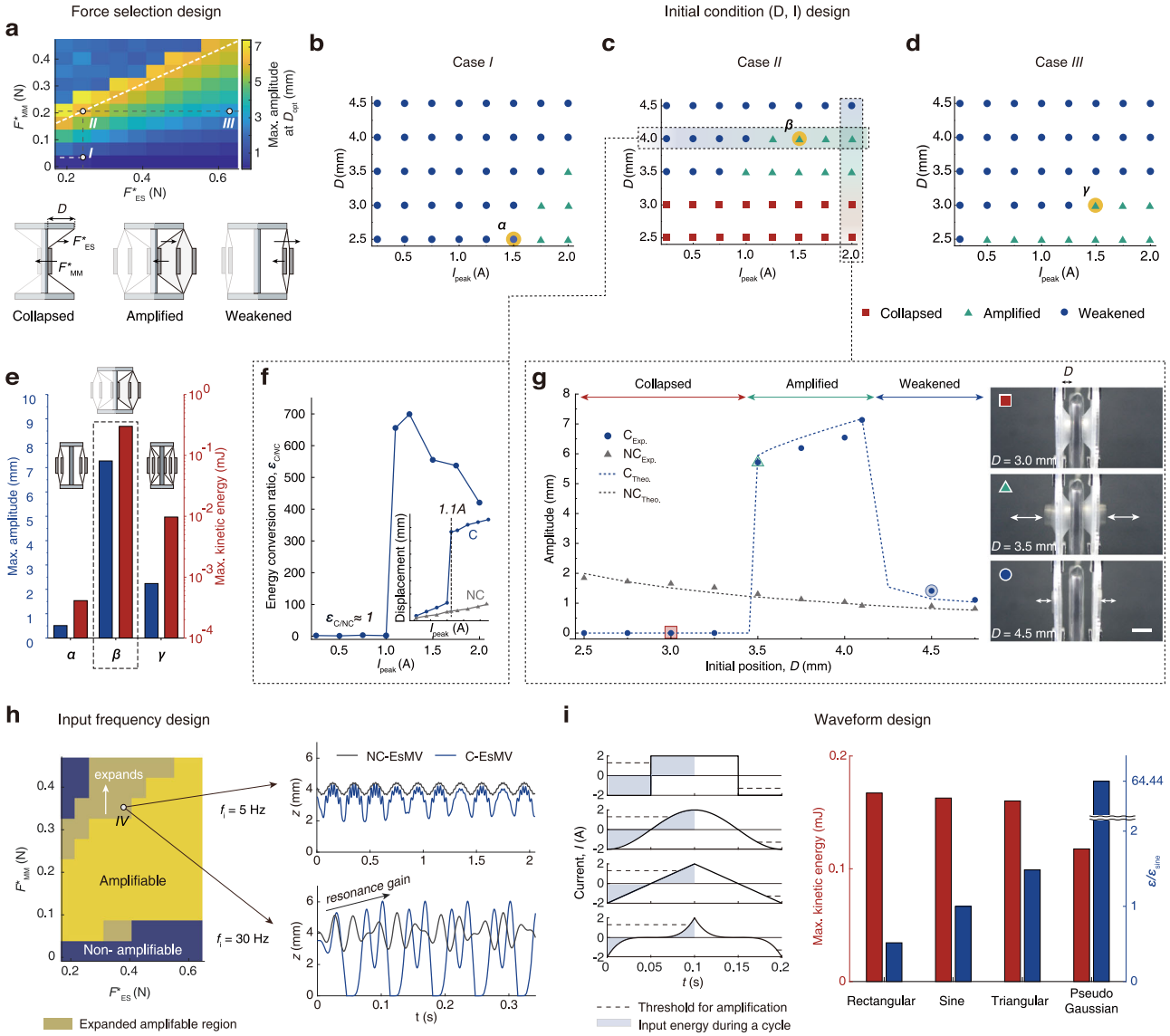

Fig. 3 | Design principles of EsMV system. a Schematic illustration of three states of C-EsMV system (*Collapsed, Weakened, and Amplified*) and a design map based on the selection of materials with characteristic forces: magnetic force, F^*_{MM}, and elastic force, F^*_{ES}. **b**–**d** State maps as a function of peak input current (I_{peak}) and initial position (D) in three cases selected from the design map: **b** *Case I*, **c** *Case II*, and **d** *Case III*. Magnetization (M) is identical across all systems, with forces controlled by the elastic modulus of the membrane (E), and the magnet thickness (h). **e** Maximum displacement and kinetic energy under optimized conditions for each case (α, β, γ) at the same peak current (I_{peak} = 1.5 A). **f** Energy ratio ($\varepsilon_{C/NC}$) between NC-EsMV and C-EsMV systems as a function of I_{peak} with a fixed D (4.0 mm). **g** Amplitude as a function of D at constant I_{peak} (2.0 A) in each system. In C-EsMV, amplitude is divided into three distinct states unlike NC-EsMV, as shown in the snapshots. Dots represent experimental data, and dashed lines indicate simulations. Scale bar, 5 mm. **h** Effect of input frequencies. At f_i = 30 Hz, systems near resonance transition from the weakened state to the amplified state, expanding the amplifiable region. **i** Effect of waveform types on actuation efficiency. As the input signal becomes more concave, the required input energy for amplification is significantly reduced, greatly improving efficiency compared to sine waves (~ 64 times).

Frequency effect on system design

While a higher input current magnitude can extend the range over which amplification occurs (Supplementary Fig. 15), the associated increase in energy consumption constrains its practical applicability. An alternative strategy is to tune the input frequency to the membrane's natural frequency, taking advantage of near-resonance behavior (Fig. 3h). Under near-resonant conditions, some systems that previously exhibited weakened vibrations—which could not be amplified, even at optimal initial position—transition to amplified vibrations, expanding the amplifiable range (ΔD). For example, *Case IV* (F^*_{ES} = 0.3870 N, F^*_{MM} = 0.3463 N), indicated in Fig. 3h, behaves similarly to NC-EsMV at 5 Hz but switches to an amplified state when the input frequency approaches the membrane's natural frequency, 30 Hz, due to resonance gain (Supplementary Fig. 16). It is worth noting that this resonance-induced amplification strongly depends on the viscoelasticity of the membrane. As shown in Supplementary Fig. 17, at the dynamic viscosity used in our experiments (η = 50 Pa·s, η/E = 0.001 s), a system that exhibited weakened vibration at 5 Hz transitioned to a stable, resonance-driven amplified vibration at 30 Hz. When the dynamic viscosity was increased by one or more orders of magnitude, the amplification effect progressively diminished, and at high damping (η = 50,000 Pa·s, η/E = 1 s) the resonance response nearly disappeared.

https://doi.org/10.1038/s41467-025-68225-y

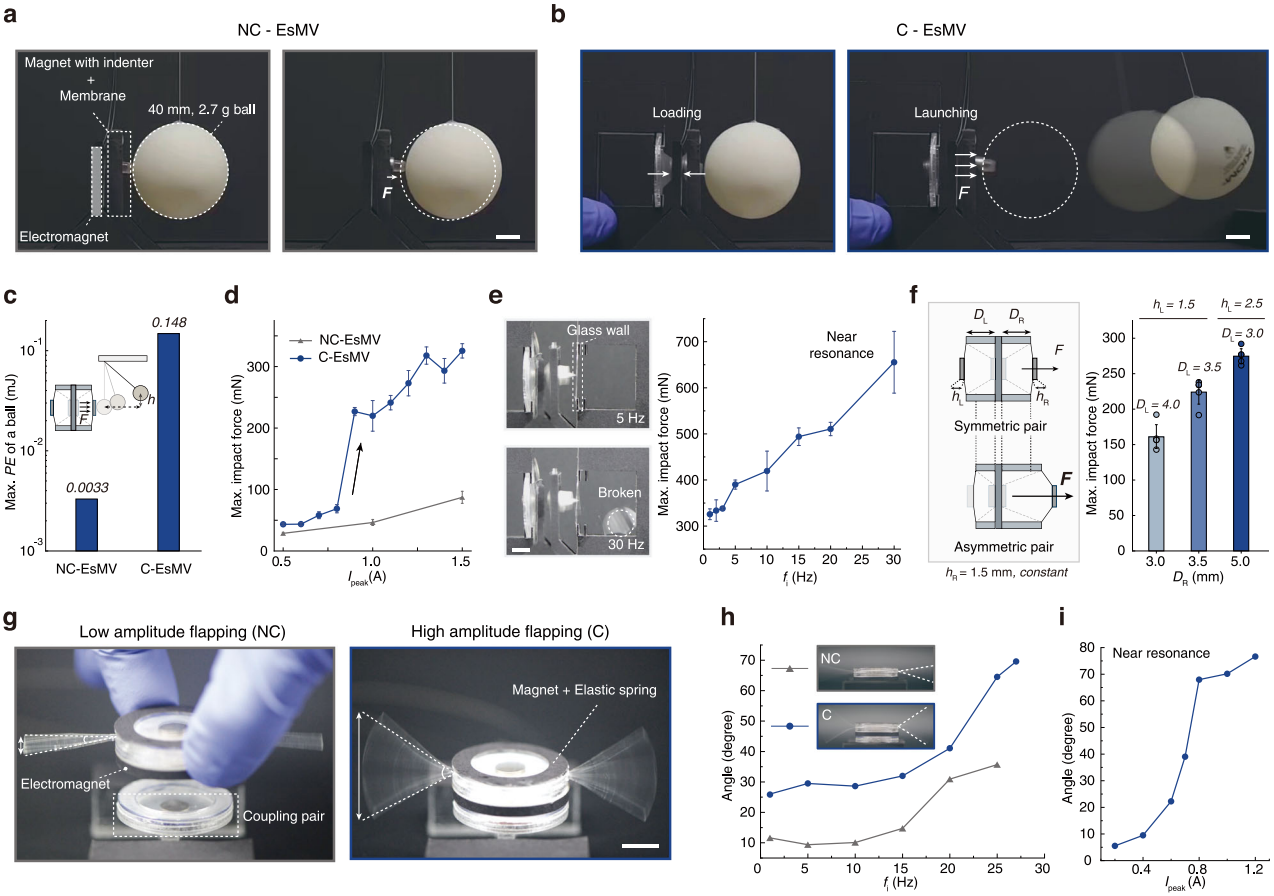

Fig. 4 | Amplification of mechanical forces and displacements in EsMV actuators. a, **b** Launching a ball in each system, **a** NC-EsMV and **b** C-EsMV. Despite identical energy input (I_{peak} = 1.0 A), greater elastic energy stored in the membrane results in a more forceful launch in the coupled system (Scale bar = 1 cm). **c** Maximum potential energy of the ball in two systems. **d** Maximum impact force as a function of input current in each system (f_i = 1 Hz). **e** Input frequencies effect on impact forces. As the frequency approaches the resonance, maximum impact force is increased, leading to a breaking of glass (0.1 mm) at higher frequencies (f_i = 30 Hz, I_{peak} = 1.5 A). Scale bar, 5 mm. **f** Geometric asymmetry effect on impact forces. As the initial position on the right side (D_R) between the magnet and electromagnet increases, controlling the left position (D_L) and the thickness of magnets (h_L, h_R) modulates vibration amplifications. **g** The flutter of wings with a NC-EsMV actuator and a C-EsMV actuator. Scale bar, 1 cm. **h** The angle of the flapping as a function of frequency in each system. Inset snapshots show the motion of flapping at each system near its resonance frequency ($f_{i,\,NC}$ = 25 Hz, $f_{i,\,C}$ = 27 Hz). **i** The angle of the flapping as a function of input current in C-EsMV actuator operating near resonance ($f_{i,\,C}$ = 27 Hz). In all experiments, error bars denote SDs; n = 5.

Designing waveforms for system efficiency

The energy conversion efficiency of the system—defined as the ratio of the maximum kinetic energy of the vibrating magnet to the supplied electrical energy—is relatively low (< 1%) because of the limited coil turns and associated geometric factors of the electromagnet. However, this efficiency can be substantially enhanced by waveform design (Supplementary Note 6 and Fig. 3i), as the waveform shape directly affects the input energy required for amplified vibrations. We numerically simulated a wide range of waveforms, spanning from convex (rectangular) to concave (pseudo-gaussian) upward. Convex-shaped waveforms facilitate rapid electromagnetic repulsion, with rectangular waveforms achieving the earliest take-off and longest duration before landing (see Supplementary Fig. 18). In contrast, concave-shaped waveforms delay the current rise to the threshold, postponing the onset of take-off. However, as long as the peak current exceeds the threshold, amplification occurs regardless of waveform shape. Notably, concave waveforms, particularly pseudo-gaussian type, offer significantly higher energy conversion efficiency because of reduced energy consumption. Simulations show that a pseudo-gaussian waveform can improve efficiency by roughly 64.4 times compared to a sine wave ($\varepsilon/\varepsilon_{sine}$), confirming the potential for more efficient operation through deliberate input waveform design.

Amplification in force and displacement

We demonstrate the utility of this mechanism in amplifying both force and displacement. We created a slingshot-like system by attaching an indenter, serving as a hammerhead, to the vibrating magnet to strike a target object. A ball (40 mm in diameter, 2.7 g in mass) was placed in contact with the indenter (Fig. 4a, b). Under NC-EsMV, limited energy transfer resulted in minimal displacement. In contrast, C-EsMV rapidly transferred energy to the ball, utilizing the nonlinear, stepwise release mechanism, propelling it substantially farther. Consequently, the ball's maximum potential energy ($P.E. = mgh$) jumped from 0.0033 mJ (NC-EsMV) to 0.148 mJ (C-EsMV)—a 50-fold improvement (Fig. 4c).

To quantify impact force, we measured the force exerted by the vibrating magnet (Supplementary Fig. 19). NC-EsMV produced a relatively small force (F_{peak} ~ 87 mN at I_{peak} = 1.5 A) that scaled linearly with the input current. C-EsMV showed a nonlinear response, with the force rising from 68 mN at I_{peak} = 0.8 A to over 225 mN at I_{peak} = 0.9 A (1 Hz, Fig. 4d), releasing stored elastic energy at a high rate over a short period, resulting in high power output. Operating near resonance further magnified the impact force as the frequency varies from 1 to 30 Hz at a fixed current (I_{peak} = 1.5 A), the maximum impact force increased from approximately 300 mN to 650 mN (Fig. 4e). At lower frequencies, the force was insufficient to break a thin glass wall

(0.1 mm thickness), but at 30 Hz, the vibrating magnet fitted with a beak-shaped indenter successfully shattered the glass wall. Beyond resonance, vibration amplitude and impact force diminished markedly.

So far, we have presented C-EsMV systems with symmetric magnet-membrane coupling. Asymmetric vibrations can also be realized by altering system geometry, material properties (*M, E*), or magnet's initial position (*D*) (Supplementary Fig. 20). Such asymmetry leads to an unequal distribution of elastic potential energy, influencing both the amplifiable range and the amplitude. Increasing distance D_R on one side under the same energy input (I_{peak} = 1.0 A) asymmetrically raises stored elastic energy, thereby boosting the maximum impact force and demonstrating the system's adaptability in tuning impact dynamics (Fig. 4f). To maintain overall balance, the opposite side was adjusted by increasing its magnet thickness and reducing its gap, compensating for the weakened magnetic attraction. Each configuration was tested as an independent system, confirming that asymmetric coupling can effectively localize and enhance actuation on a chosen side.

Beyond force amplification, the amplified vibration can be converted to large fluttering motions (Fig. 4g). By attaching wings (PET, 0.1 mm thickness) to the magnet in a lever-like configuration (Supplementary Fig. 21), the C-EsMV system achieved significantly larger wing flaps than NC-EsMV system, quantified by angular displacement (θ) from 1 Hz to near resonant frequency, 27 Hz (Fig. 4h and Supplementary Video 6). Even under near resonant conditions, the flapping amplitude of C-EsMV exhibited a nonlinear response to the applied current (Fig. 4i).

Mechanical memory

The ability of mechanical systems to autonomously respond to external stimuli, exhibiting embodied physical intelligence without the need for programmed controls, is of great interest[42,43]. Building on the nonlinear hysteretic behavior and the "shooting" phenomenon of C-EsMV, we introduce a concept of mechanical memory with exteroceptive characteristics (Fig. 5a) requiring no complex manipulation. By replacing the rigid spacer with an elastic spacer, which can deform and recover when subjected to external triggers, the system transitions from a weakened vibration state (*standby*) to an amplified vibration state (*memorized*) whenever the spacer is compressed, drawing the magnets closer and producing a "mechanical shooting" effect (Supplementary Fig. 22). This process is analogous to the electrical shooting described earlier, relying on inertia–elastic energy exchange that drives the transition from the weakened to the amplified vibration state (Supplementary Fig. 23). Once triggered, the system sustains oscillation within the amplified branch even after the external input is removed. As shown in Supplementary Fig. 24, this design effectively stores external mechanical stimuli as persistent amplified vibrational states—a phenomenon we term mechanical memory.

We characterize this mechanical memory using four regimes (*R1, R2, R3*, and *R4*) defined by characteristic currents on a current-amplitude hysteresis graph (Fig. 5b): $I_{th,\ off}$, $I_{ext.cept}$, and $I_{th,\ on}$. As shown in Fig. 5c, d, Regime 1 (*R1*, $I < I_{th,\ off}$) requires significant trigger force and displacement for amplified vibration, but immediately reverts to *standby* when the trigger is removed, preventing memorization. Regimes 2 (*R2*) and 3 (*R3*) lie within the exteroceptive range, each exhibiting distinct memory behaviors. In *R2* ($I_{th,\ off} < I < I_{ext.cept}$), memory retention is positively correlated with the trigger duration, creating a "volatile memory mode" where *memorized* states eventually reset. In *R3* ($I_{ext.cept} < I < I_{th,\ on}$), brief mechanical triggers induce permanent amplified vibration, defining a "non-volatile memory mode". Regime 4 (*R4*, $I > I_{th,\ on}$) allows amplified vibration without any trigger (Fig. 5c, Supplementary Fig. 25, and Supplementary Video 6).

We evaluated the trigger force (F_T) and trigger displacement (D_T) required for activation (Fig. 5e, corresponding to Supplementary Fig. 9e). At currents above $I_{th,\ on}$ *(R4),* F_T and D_T are zero because amplification occurs spontaneously. As the current decreases further below $I_{th,\ on}$ (*R3 ~ R1*), greater trigger force and displacement are needed. For example, at I_{peak} = 1.5 A, the system can be activated with a minimal force ($F_T \approx 0.17$ N) and displacement ($D_T \approx 0.5$ mm). Consequently, modulating I_{peak} allows tuning of trigger sensitivity, while varying the modulus of the elastic spacer provides additional control over the activation requirements (Supplementary Fig. 26).

To assess the longevity of the triggered amplification after the trigger is removed, we measured retention time (t_R) (Fig. 5f). In *R4*, amplification is perpetual and does not depend on a trigger. In *R3*, even a brief trigger (trigger time, $t_T < 0.1$ s) induces indefinite amplified vibration, demonstrating non-volatile memory. However, the duration of this non-volatile retention is governed by the viscoelastic property of the membrane (Supplementary Fig. 27): higher viscosity increases damping and gradually suppresses sustained oscillations, whereas a more elastic membrane maintains stable amplified vibration. This confirms that membrane elasticity is essential for robust memory retention. In *R2*, retention depends on how long the trigger is applied—short triggers (t_T = 0.1 s) cause rapid decay, while relatively longer triggers (t_T = 10 s) extend retention to nearly 6 s. This volatile nature arises from membrane resonance gains and the elastic spacer's relaxation time, enabling tunable memory retention. In *R1*, the system immediately returns to *standby* once the trigger is removed.

To visualize mechanical memory as a trigger tracer, we built a 3 × 3 array of independent C-EsMV units (Fig. 5g). In the volatile mode, applying a 15 s trigger to one cell (C1) and a 7 s trigger to another (C9) yields retention times of 7 s and 1.5 s, respectively. (Fig. 5h, top). In the non-volatile mode, cells were sequentially activated in a programmed pattern, maintaining amplified vibration indefinitely (Fig. 5h, bottom and Supplementary Video 7). The system can be reset through external interventions, such as touching the vibrating magnet to dissipate its kinetic energy (Supplementary Fig. 28).

Since the memory effect relies on bistable, hysteretic response of the membrane-magnet composites, applying force directly to the magnet rather than the spacer produces the same outcome (Supplementary Fig. 29). In addition to the non-contact trigger-based memory described earlier (Fig. 1h), any mechanical trigger that gives additional elastic energy can utilize this mechanism, broadening the potential applications of this mechanical memory across diverse environments.

Discussion

The proposed C-EsMV system leverages magnetic attraction and elastic regulation to induce Elasto-Magnetic Instability (EsMI), enabling amplified inertial motion through a simple and scalable mechanism. This dynamic collapse, governed by the interplay between elastic and magnetic forces, leads to vigorous vibrations and efficient energy release, achieving up to a 700-fold increase in energy efficiency relative to the NC-EsMV system.

By systematically tuning magnetic and elastic parameters, we establish design principles—summarized in the design map—that generalize across different force scales. Inertia-driven dynamics enhance two key features: nonlinear response and hysteretic behavior, enabling stepwise force and motion output. These behaviors are demonstrated in applications such as slingshot-like actuation, wing flutter, and mechanical memory with either volatile or non-volatile characteristics.

While conventional electromagnetic actuators are designed to maximize force and speed, their efficiency typically declines at high currents, limiting their integration into compact systems. In contrast, the C-EsMV system offers an alternative approach that enables energy-efficient, stepwise responses suitable for space- and power-constrained environments. Moreover, because the underlying instability mechanism is not limited to electromagnetic control, it may be extended to other forms of actuation, including pneumatic and

https://doi.org/10.1038/s41467-025-68225-y

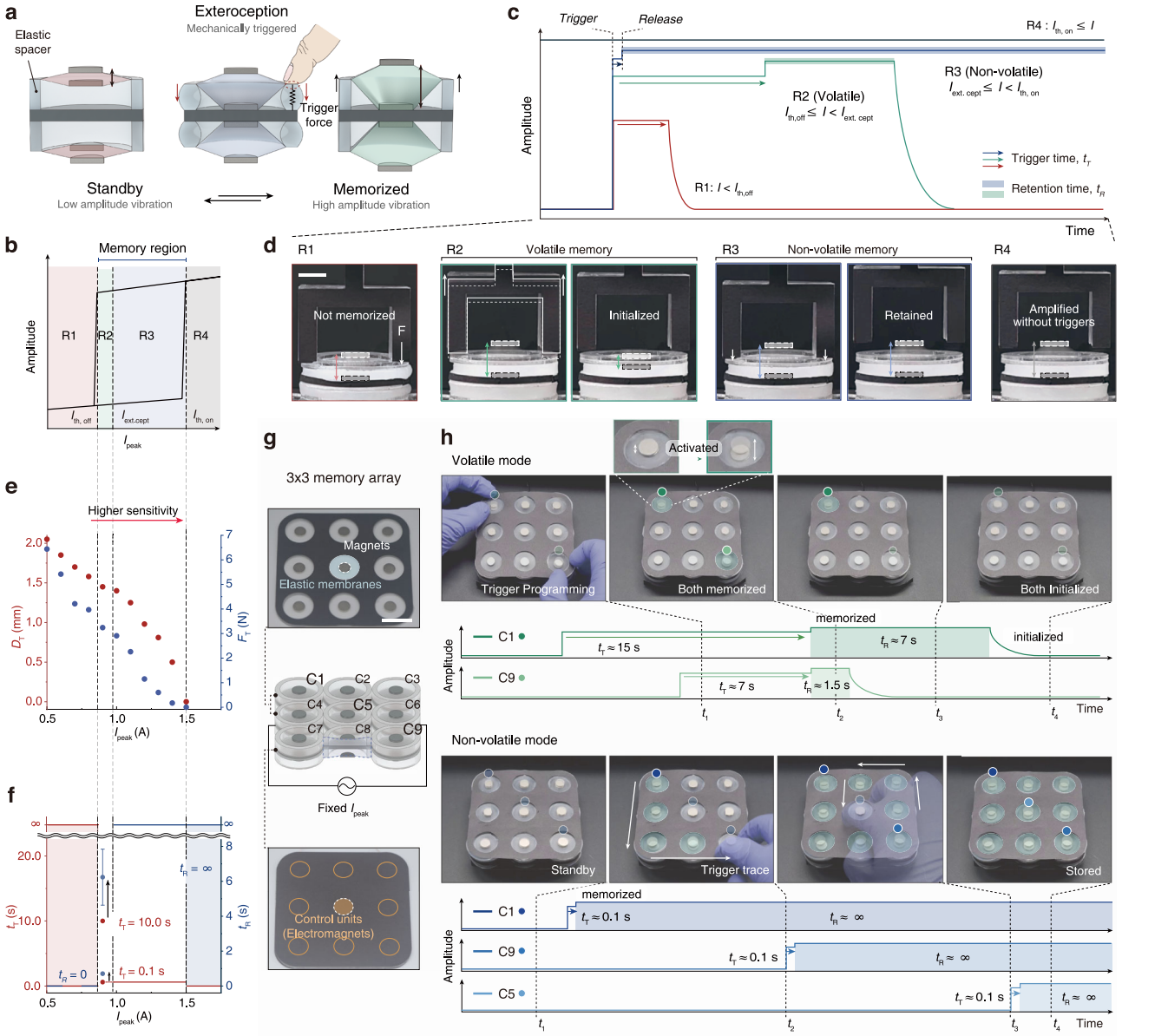

Fig. 5 | Volatile and non-volatile memories operated by a mechanical triggering. a Schematic illustration of mechanical memory using C-EsMV. **b**–**d** Behavior of mechanical memory: **b** Schematic graph of hysteretic motion as a function of current, with the system divided into four regimes based on three characteristic currents ($I_{th,\,off}$, $I_{ext.cept}$, $I_{th,\,on}$). **c** Vibration amplitude over time in each regime. In *R1* ($I < I_{th,\,off}$) and *R2* ($I_{th,\,off} \leq I < I_{ext.cept}$), the system exhibits volatility, with retention possible only in *R2*. In *R3* ($I_{ext.cept} \leq I < I_{th,\,on}$), non-volatility is observed, maintaining amplified vibration indefinitely after triggering. In *R4* ($I_{th,\,on} \leq I$), amplification occurs without a trigger. **d** Representative vibration behaviors in each region. Scale bar, 8 mm. **e** Trigger force (F_T) and displacement (D_T) required for memorization in each regime. **f** Retention time (t_R), indicating how long the system retains the amplified vibration after the trigger is removed. It is shown as a function of trigger duration (t_T) in each regime. Error bars denote SDs; $n = 5$. **g** Structure of 3 × 3 array units for a mechanical trigger "tracer" composed of elastomer membranes, coupled magnets, and electromagnets (Scale bar = 2 cm). **h** Function of volatile and non-volatile memory modes over time based on the amplitude. Volatile mode operates at $I_{peak} = 0.9$ A in *R2*, while non-volatile mode is activated at $I_{peak} = 1.1$ A in *R3*. Both functions are demonstrated at $f_i = 30$ Hz.

chemical triggers. The demonstrated ability of the C-EsMV system to achieve nonlinear amplification and motion hysteresis highlights a broader design framework for adaptive mechanical systems. This approach may be particularly suited for scenarios that require discrete, energy-efficient responses to small stimuli with programmable thresholds—such as mechanical transistors, spike-signal processors, or memory-integrated devices. More broadly, these finding suggest that embedding inertia as an active design element in instability-driven architectures provides a distinct and versatile route toward programmable, efficient, and compact actuation systems.

Methods

Fabrication of EsMV system

Both NC-EsMV and C-EsMV systems utilized identical NdFeB permanent magnets (Jungsin Corp.) and electromagnets (TDK Corp., WR151580-48F2-G). The permanent magnets (radius = 4 mm, thickness = 0.5 mm, three-layer stack) exhibit a typical magnetization of $M_a = M_b = 4 \times 10^5$ A/m, which was experimentally verified by measuring the magnetic attraction force as a function of distance. This magnetization value was consistently used in both experiments and simulations. Elastic membranes were custom-fabricated using spin coating (Dong Ah Trade Corp, ACE-200) on a Teflon substrate to ensure uniform thickness. Coated elastomers were cured at 60 °C for 1 h.

Membranes were pre-stretched using an acrylic frame at specified stretch ratios ($\lambda = 1.5$) to adjust elastic forces. Donut-shaped acrylic spacers, cut with a laser cutter (Universal Laser System, VLS3.50), were attached to the pre-stretched membranes to control the distance between the electromagnet and the magnet, i.e., initial position D. In NC-EsMV, the assembly (magnet + membrane + spacer) was mounted on one side of the electromagnet. For C-EsMV system, an identical assembly was symmetrically added to the opposite side of the electromagnet.

Measurement of the real-time position of the vibrating magnet

To analyze magnet motion during vibration, an acrylic-based indenter (0.1 g) with a red marker was attached to the vibrating magnet. Motion was recorded using a high-speed camera (Phantom, V611-32G-MAG) at various driving frequencies. Magnet position was tracked using custom MATLAB code, and the amplitude, velocity was obtained by differentiating the position data with respect to time.

Characterization of elastic membranes and magnets, and basic force measurement

Three elastomer types with varying moduli (Smooth-On Inc., EcoFlex 0020, EcoFlex 0050, Dragon Skin NV10) were used. Elastomers were prepared by mixing parts A and B in a 1:1 ratio per supplier instructions. Membranes were pre-stretched and tested for elastic restoration forces by pressing the center of the membrane using a universal testing machine (Instron 3343). Magnetic forces were controlled by stacking magnets (0.5 mm thick, 8 mm diameter). Magnet-magnet forces were measured by fixing one magnet to the base of the testing machine and recording the force required to detach another magnet. Similarly, electromagnet-magnet forces were measured by fixing the electromagnet to the base and recording forces at various currents. Key parameters, including E, c, M_a, and M_b, were extracted through the experiments and applied to the analytical model. The predicted force profiles closely matched the measured results (Supplementary Fig. 2b–d).

Construction of state regime map for various magnetic and elastic conditions

The electromagnet was fixed in the center, with a linear stage (Pinetek, PX30-CL15) on each side. Each stage held a pre-stretched membrane and an attached magnet, enabling precise control of initial position (D) between the electromagnet and the magnet-membrane pairs. This setup allowed identification of system's three states—*collapsed, amplified*, and *weakened*—represented in state regime map (Fig. 3b–d).

Electrical input source characterization

To drive the EsMV systems, a function generator (Agilent, 33612A) was used to produce various waveforms (sine/rectangular/triangular). A current amplifier (ACCEL Instruments, TS250-0) or DC power supply (Keysight, E36233A), combined with custom circuit amplifier (OPA541), delivered the required current for experiments.

Measurement of trigger force and displacement in mechanical memory

Elastic spacers were fabricated using molding processes with elastomers of different moduli (EcoFlex 0020 and Elite Double, Zhermack) (Supplementary Fig. 26). Trigger force, trigger displacement (the pressing distance needed for amplification), and retention time (the duration of amplified vibration after trigger) were quantified using a universal testing machine. This setup controlled pushing speed, hold time, and retraction speed, enabling measurements across different mechanical memory regimes (Supplementary Fig. 25).

Data availability

All data supporting the findings of this study are provided with the paper, including in the Source Data and Supplementary Information. Source data are provided with this paper.

References

1. Pal, A., Restrepo, V., Goswami, D. & Martinez, R. V. Exploiting mechanical instabilities in soft robotics: control, sensing, and actuation. *Adv. Mater.* **33**, 2006939 (2021).
2. Choi, W. et al. A hyperelastic torque-reversal mechanism for soft joints with compression-responsive transient bistability. *Sci. Robot.* **10**, eado7696 (2025).
3. Chi, Y. et al. Bistable and multistable actuators for soft robots: structures, materials, and functionalities. *Adv. Mater.* **34**, 2110384 (2022).
4. Forterre, Y., Skotheim, J. M., Dumais, J. & Mahadevan, L. How the venus flytrap snaps. *Nature* **433**, 421–425 (2005).
5. Watkinson, S. C., Boddy, L. & Money, N. *The Fungi* (Academic, London, 2015).
6. Vincent, O. et al. Ultra-fast underwater suction traps. *Proc. R. Soc. B: Biol. Sci.* **278**, 2909–2914 (2011).
7. Westermeier, A. S. et al. How the carnivorous waterwheel plant (Aldrovanda vesiculosa) snaps. *Proc. R. Soc. B: Biol. Sci.* **285**, 20180012 (2018).
8. Li, C. Y. et al. Spontaneous and rapid electro-actuated snapping of constrained polyelectrolyte hydrogels. *Sci. Adv.* **8**, eabm9608 (2022).
9. Wang, X. et al. Fracture-driven power amplification in a hydrogel launcher. *Nat. Mater.* **23**, 1428–1435 (2024).
10. Wang, Y. et al. Insect-scale jumping robots enabled by a dynamic buckling cascade. *PNAS* **120**, e2210651120 (2023).
11. Chi, Y., Hong, Y., Zhao, Y., Li, Y. & Yin, J. Snapping for high-speed and high-efficient butterfly stroke–like soft swimmer. *Sci. Adv.* **8**, eadd3788 (2022).
12. Gorissen, B., Melancon, D., Vasios, N., Torbati, M. & Bertoldi, K. Inflatable soft jumper inspired by shell snapping. *Sci. Robot.* **5**, eabb1967 (2020).
13. Kim, Y., van den Berg, J. & Crosby, A. J. Autonomous snapping and jumping polymer gels. *Nat. Mater.* **20**, 1695–1701 (2021).
14. Tang, Y. et al. Leveraging elastic instabilities for amplified performance: spine-inspired high-speed and high-force soft robots. *Sci. Adv.* **6**, eaaz6912 (2020).
15. Chen, T., Bilal, O. R., Shea, K. & Daraio, C. Harnessing bistability for directional propulsion of soft, untethered robots. *PNAS* **115**, 5698–5702 (2018).
16. Baumgartner, R. et al. A lesson from plants: high-speed soft robotic actuators. *Adv. Sci.* **7**, 1903391 (2020).
17. Hines, L., Petersen, K. & Sitti, M. Inflated soft actuators with reversible stable deformations. *Adv. Mater.* **28**, 3690–3696 (2016).
18. Tian, Y. et al. A dynamically programmable hydrogel surface with rapid magnetically actuated snapping of bistable dome configurations. *Adv. Funct. Mater.* **35**, 2508885 (2025).
19. van Laake, L. C., de Vries, J., Kani, S. M. & Overvelde, J. T. A fluidic relaxation oscillator for reprogrammable sequential actuation in soft robots. *Matter* **5**, 2898–2917 (2022).
20. Rothemund, P. et al. A soft, bistable valve for autonomous control of soft actuators. *Sci. Robot.* **3**, eaar7986 (2018).
21. Conrad, S. et al. 3D-printed digital pneumatic logic for the control of soft robotic actuators. *Sci. Robot.* **9**, eadh4060 (2024).
22. Djellouli, A. et al. Shell buckling for programmable metafluids. *Nature* **628**, 545–550 (2024).
23. Jin, L. et al. Guided transition waves in multistable mechanical metamaterials. *PNAS* **117**, 2319–2325 (2020).
24. Chen, T., Pauly, M. & Reis, P. M. A reprogrammable mechanical metamaterial with stable memory. *Nature* **589**, 386–390 (2021).

25. Preston, D. J. et al. A soft ring oscillator. *Sci. Robot.* **4**, eaaw5496 (2019).
26. Rafsanjani, A., Zhang, Y., Liu, B., Rubinstein, S. M. & Bertoldi, K. Kirigami skins make a simple soft actuator crawl. *Sci. Robot.* **3**, eaar7555 (2018).
27. Shin, G. et al. Soft electromagnetic artificial muscles using high-density liquid-metal solenoid coils and bistable stretchable magnetic housings. *Adv. Funct. Mater.* **34**, 2302895 (2024).
28. Tang, D. et al. Bistable soft jumper capable of fast response and high takeoff velocity. *Sci. Robot.* **9**, eadm8484 (2024).
29. Shao, H., Wei, S., Jiang, X., Holmes, D. P. & Ghosh, T. K. Bioinspired electrically activated soft bistable actuators. *Adv. Funct. Mater.* **28**, 1802999 (2018).
30. Patel, D. K. et al. Highly dynamic bistable soft actuator for reconfigurable multimodal soft robots. *Adv. Mater. Technol.* **8**, 2201259 (2023).
31. Hao, X. P. et al. Kirigami-design-enabled hydrogel multimorphs with application as a multistate switch. *Adv. Mater.* **32**, 2000781 (2020).
32. Steinhardt, E. et al. A physical model of mantis shrimp for exploring the dynamics of ultrafast systems. *PNAS* **118**, e2026833118 (2021).
33. Ilton, M. et al. The principles of cascading power limits in small, fast biological and engineered systems. *Science* **360**, eaao1082 (2018).
34. Habib, G. Predicting saddle-node bifurcations using transient dynamics: a model-free approach. *Nonlinear Dyn* **111**, 20579–20596 (2023).
35. Rega, G. Nonlinear dynamics in mechanics: state of the art and expected future developments. *J. Comput. Nonlinear Dyn.* **17**, 080802 (2022).
36. Acome, E. et al. Hydraulically amplified self-healing electrostatic actuators with muscle-like performance. *Science* **359**, 61–65 (2018).
37. Bujard, T., Giorgio-Serchi, F. & Weymouth, G. D. A resonant squid-inspired robot unlocks biological propulsive efficiency. *Sci. Robot.* **6**, eabd2971 (2021).
38. Kobayashi, M. & Abe, J. Optical motion control of maglev graphite. *J. Am. Chem. Soc.* **134**, 20593–20596 (2012).
39. Lee, B. et al. High-performance compliant thermoelectric generators with magnetically self-assembled soft heat conductors for self-powered wearable electronics. *Nat. Commun.* **11**, 5948 (2020).
40. Yoder, Z., Rumley, E. H., Schmidt, I., Rothemund, P. & Keplinger, C. Hexagonal electrohydraulic modules for rapidly reconfigurable high-speed robots. *Sci. Robot.* **9**, eadl3546 (2024).
41. Gu, H. et al. Self-folding soft-robotic chains with reconfigurable shapes and functionalities. *Nat. Commun.* **14**, 1263 (2023).
42. Zhao, Y. et al. Twisting for soft intelligent autonomous robot in unstructured environments. *PNAS* **119**, e2200265119 (2022).
43. Polat, D. S., Chen, Z., Weima, S. A., Aya, S. & Liu, D. An autonomous snapper featuring adaptive actuation and embodied intelligence. *Sci. Adv.* **11**, eadu4268 (2025).

Acknowledgements

This work was supported by a National Research Foundation of Korea (NRF) grant funded by the Korean Government (No. RS-2024-00459269 and 2018-052541).

Author contributions

S.-Y.C., J.-S.P., and J.-Y.S. conceived the idea and wrote the manuscript. S.-Y.C. and J.-S.P. designed, conducted, analyzed the experiments. J.-S.P. developed the theoretical modeling and performed simulations. W.J.S., M.K., Y.H.L., Y.E.C., and H.L. supported demonstrations and video recordings. All authors discussed the results and commented on the manuscript. J.-Y.S. and H.-Y.K. supervised the study.

Competing interests

The authors declare no competing interests.

Additional information

Supplementary information The online version contains supplementary material available at https://doi.org/10.1038/s41467-025-68225-y.

Correspondence and requests for materials should be addressed to Ho-Young Kim or Jeong-Yun Sun.

Peer review information *Nature Communications* thanks Jingda Tang, Zi Liang Wu, and the other anonymous reviewer(s) for their contribution to the peer review of this work. A peer review file is available.

Supplementary Information for

Elasto-magnetic instabilities for amplified actuation and mechanical memory

Seong-Yu Choi[1]†, Ji-Sung Park[2,3]†, Won Jun Song[1], Maga Kim[1], Yun Hyeok Lee[1], Yong Eun Cho[1], Hakjun Lee[1], Ho-Young Kim[2,4*], Jeong-Yun Sun[1,5*]

[1]Departmant of Materials Science and Engineering, Seoul National University, Seoul 08826, Republic of Korea

[2]Departmant of Mechanical Engineering, Seoul National University, Seoul 08826, Republic of Korea

[3]Institute of Mechanical Engineering, École Polytechnique Fédérale de Lausanne, 1015 Lausanne, Switzerland

[4]Institute of Advanced Machines and Design, Seoul National University, Seoul 08826, Republic of Korea

[5]Research Institute of Advanced Materials (RIAM), Seoul National University, Seoul 08826, Republic of Korea

† These authors contributed equally to this work.

Correspondence to: hyk@snu.ac.kr, jysun@snu.ac.kr

This PDF file includes:

Supplementary Note 1 to 6

Supplementary Table 1 to 2

Supplementary Figure 1 to 29

Other Supplementary Materials for this manuscript include the following:

Supplementary Videos 1 to 7

Table of contents

Supplementary Note 1. Analysis of forces acting on a magnet

We here provide details of analytical force models given in main text. We first observe a case when a membrane of Young's modulus E, Poisson's ratio ν, radius R_m, prestretch λ_p, and final thickness h_m with a magnet of radius R_a attached on the center is vertically displaced by amplitude, Δ, as depicted in Supplementary Fig. 4a. Due to axisymmetry, lateral force components cancel out, and the net force acts purely in the vertical direction. As the magnet restrains the stretching of the middle region, the stretched membrane can be modeled as a side surface of a truncated cone which allows us to express radial and circumferential stretches λ_r and λ_θ as,

$$\lambda_\mathrm{r} = \lambda_\mathrm{p}\lambda_{1,\mathrm{v}} = \lambda_\mathrm{p}\frac{\sqrt{(R_\mathrm{m}-R_\mathrm{a})^2+\Delta^2}}{R_\mathrm{m}-R_\mathrm{a}}, \qquad \lambda_\theta = \lambda_\mathrm{p}\lambda_{2,\mathrm{v}} = \lambda_\mathrm{p} \tag{1}$$

Here, $\lambda_{1,\mathrm{v}}$ and $\lambda_{2,\mathrm{v}}$ represent the additional radial and circumferential stretches, respectively, due to vertical displacement Δ, and are scaled by the initial prestretch λ_p.

Therefore, we can calculate the total strain potential energy of the membrane $E_\mathrm{ES} = A_\mathrm{ES}\frac{E}{4(1+\nu)}(\lambda_r^2+\lambda_\theta^2+\lambda_r^{-2}\lambda_\theta^{-2}-3)$ based on the neo-Hookean incompressible model[1], where A_ES is the membrane area. Substituting Eq. (1) into this relation yields:

$$E_\mathrm{ES} = \frac{\pi E}{4(1+\nu)}h_\mathrm{m}\lambda_\mathrm{p}^2(R_\mathrm{m}^2-R_\mathrm{a}^2)\left[\frac{(R_\mathrm{m}-R_\mathrm{a})^2+\Delta^2}{(R_\mathrm{m}-R_\mathrm{a})^2}+1+\frac{1}{\lambda_\mathrm{p}^6}\frac{(R_\mathrm{m}-R_\mathrm{a})^2}{(R_\mathrm{m}-R_\mathrm{a})^2+\Delta^2}-\frac{3}{\lambda_\mathrm{p}^2}\right]. \tag{2}$$

Differentiating E_ES by $z = D - \Delta$, we get the elastic membrane force F_ES as,

$$F_\mathrm{ES} = -\frac{\partial E_\mathrm{ES}}{\partial z} = \frac{\pi E}{2(1+\nu)}h_\mathrm{m}\lambda_\mathrm{p}^2(R_\mathrm{m}^2-R_\mathrm{a}^2)\left[\frac{1}{(R_\mathrm{m}-R_\mathrm{a})^2}-\frac{1}{\lambda_\mathrm{p}^6}\frac{(R_\mathrm{m}-R_\mathrm{a})^2}{((R_\mathrm{m}-R_\mathrm{a})^2+(D-z)^2)^2}\right](D-z), \tag{3}$$

where D is the initial spacing between the electromagnet and the magnet. By neglecting the higher order term and rearranging, the elastic force F_ES can be approximated as:

$$F_\mathrm{ES} = \frac{\pi E}{2(1+\nu)}h_\mathrm{m}\lambda_\mathrm{p}^2(R_\mathrm{m}+R_\mathrm{a})\frac{D-z}{R_\mathrm{m}-R_\mathrm{a}} = F_\mathrm{ES}^*\frac{D-z}{R_\mathrm{m}-R_\mathrm{a}}, \tag{4}$$

where F^*_{ES} corresponds to the magnitude of the elastic force when the membrane achieves a radial stretch $\lambda_r = \sqrt{2}$, when inclination angle (of the isosceles trapezoid formed by the membrane) reaches 45°.

The damping force F_d of the membrane is also considered. We use the Kelvin-Voigt model comprising a spring and a dashpot in parallel to describe the viscous damping effect of membrane during vibration[2].

$$F_{\mathrm{d}} = \eta \frac{\dot{\lambda_1}}{\lambda_1} = -\eta\pi\, h_{\mathrm{m}}(R_{\mathrm{m}}^2 - R_{\mathrm{a}}^2) \frac{(D-z)^2}{[(R_{\mathrm{m}} - R_{\mathrm{a}})^2 + (D-z)^2]^2} \dot{z} \tag{5}$$

where η is the viscosity, and the dot notations in $\dot{\lambda_1}$ and $\dot{z}$ denote time derivatives.

The magnet-magnet attraction force F_{MM} can be obtained by the Bio-Savart law, which is written as[3,4]

$$F_{\mathrm{M\,M}} = \frac{\mu_0}{2} M_{\mathrm{a}} M_{\mathrm{b}} R_{\mathrm{a}} R_{\mathrm{b}} \int_0^{2\pi} \cos\delta d\delta \int_{-\frac{h_{\mathrm{a}}}{2}}^{\frac{h_{\mathrm{a}}}{2}} \left[\frac{1}{\sqrt{R_{\mathrm{a}}^2 + R_{\mathrm{b}}^2 - 2R_{\mathrm{a}}R_{\mathrm{b}}\cos\delta \;\; + \left(\frac{h_{\mathrm{a}}}{2} + 2z + h - z_{\mathrm{a}}\right)^2}} \right. \tag{6}$$

$$\left. - \frac{1}{\sqrt{R_{\mathrm{a}}^2 + R_{\mathrm{b}}^2 - 2R_{\mathrm{a}}R_{\mathrm{b}}\cos\delta \;\; + \left(\frac{h_{\mathrm{a}}}{2} + 2z + h + h_{\mathrm{b}} - z_{\mathrm{a}}\right)^2}} \right] dz_{\mathrm{a}}$$

where μ_0 is the vacuum permeability, M_a and M_b are the magnetizations, R_a and R_b are the radii, h_a and h_b are the thicknesses of the magnets placed on opposite side of electromagnet, and h is the thickness of the electromagnet. To simplify notation, we group the geometric contributions into a single term $\Omega \sim f(R_{\mathrm{a}}, R_{\mathrm{b}}, h_{\mathrm{a}}, h_{\mathrm{b}}, h, z)$, and express the force compactly as: $F_{\mathrm{M\,M}} = \frac{\mu_0}{2} M_{\mathrm{a}} M_{\mathrm{b}} \Omega$.

Characteristic value $F^*_{\mathrm{M\,M}} = \frac{\mu_0}{2} M_{\mathrm{a}} M_{\mathrm{b}} \Omega|_{z=0}$ is numerically determined by evaluating Eq. (6) when the magnets are positioned at the bottom surface of the electromagnet to standardize the magnet strength of varying geometries.

The electromagnetic force F_{EM} between the electromagnet and the magnet on one side (denoted by subscript a for clarity) is given by the summation of those from circular current loop in radial and longitudinal directions[3,4]:

$$F_{\mathrm{EM}} = \frac{\mu_0}{2} M_{\mathrm{a}} R_{\mathrm{a}} I \sum_{j=1}^{n_{\mathrm{s}}} \sum_{i=1}^{n_{\mathrm{t}}} \int_0^{2\pi} r_i \cos\delta \left[\frac{1}{\sqrt{R_{\mathrm{a}}^2 + r_i^2 - 2R_{\mathrm{a}} r_i \cos\delta \ + \left(h_j + z\right)^2}} \right. \\ \left. - \frac{1}{\sqrt{R_{\mathrm{a}}^2 + r_i^2 - 2R_{\mathrm{a}} r_i \cos\delta \ + \left(h_{\mathrm{a}} + z + h_j\right)^2}} \right] d\delta \tag{7}$$

where I is the current, n_{s} and n_{t} are the number of coil turns and layers, respectively, r_i is the radius of i^{th} coil, and h_j is the height gap of the j^{th} coil layer. Magnetic and electromagnetic potential energies were calculated by integrating each force acting on the magnet over the displacement ($\int F \mathrm{d}z$).

We neglect the gravitational force and external damping by ambient air. The gravitational force $F_{\mathrm{g}} = m\,g \approx (10^{-4}\ \mathrm{kg})(10\ \mathrm{m/s^2}) \approx 10^{-3}$ N and the form drag $F_{\mathrm{fl}} = \frac{1}{2} C_D \rho_a A v^2 \approx \frac{1}{2}(1)(1.2\ \mathrm{kg/m^3})(10^{-4}\ \mathrm{m^2})(0.5\ \mathrm{m/s})^2 \approx 10^{-5}$ N are both insignificant compared to other forces, which are on the order of 10^{-1} N. In effect, the structure showed consistent performance in both horizontal and vertical orientations.

Using the defined force components, the equations of motion for the magnet are numerically solved in MATLAB based on Newton's second law:

$$m\ddot{z} = F_{\mathrm{ES}} - F_{\mathrm{M\,M}} - F_{\mathrm{EM}} - F_{\mathrm{d}}, \tag{8}$$

where m is the mass of a single magnet. The kinetic energy of the magnet was determined using the numerically obtained velocity, given by $\frac{1}{2}mv^2$. The membrane's mass is neglected due to its relatively small contribution. Once the magnets collapse onto the electromagnet surface, we assume an inelastic collision and reset the magnet's velocity to zero. Variations in the coefficient of restitution have minimal influence on the system's overall dynamics, owing to the dominant magnetic attraction. Key experimental parameters, including E, η, M_{a}, and M_{b}, are independently measured and detailed in the Methods section of the main text. The geometric and electrical specifications of the electromagnet used throughout the study are listed in Table 1.

For the system corresponding to Fig. 2, we use elastic membrane of Ecoflex50 of initial thickness 0.33 mm with prestretch λ_{p} = 1.5 (final thickness h_{m} = 0.147 mm) and radius R_{m} = 10 mm. The moving magnets have the total thickness $h_{\mathrm{a}} = h_{\mathrm{b}}$ = 1.5 mm (by stacking three 0.5 mm magnets) and radii $R_{\mathrm{a}} = R_{\mathrm{b}}$ = 4 mm, made of neodymium with

density ρ = 7500 kg/m^3. Extra acrylic spacers of 0.7 mm were attached on both top and bottom of the electromagnet to control peak magnetic forces.

Table 1. Experimental parameters of the electromagnet

Variable name	Value
R_{EM}	0.5 Ω
n_{s}	11
n_{t}	4
$r_{i,\mathrm{inner}}$	2.4 mm
$r_{i,\mathrm{outer}}$	6.4 mm
h_1	0.2 mm
h_2	0.6 mm
h_3	1.0 mm
h_4	1.4 mm

Supplementary Note 2. Static force analysis

As shown in Supplementary Fig. 2a, the current applied to the electromagnet produces a corresponding magnetic field. During the half-cycle from the point of maximum repulsive force at t_0 to the point of maximum attractive force at t_2, we analyzed the forces exerted on the magnet. In NC-EsMV, at $t = t_0$, the electromagnet pushes the magnet to its farthest position. At $t = t_2$, the electromagnet pulls the magnet to its closest position (Supplementary Fig. 2b). These forces vary with the distance (z) between the magnet and the electromagnet. Depending on the polarity of the alternating current (AC) input, the electromagnetic force alternates between repulsive ($F_{EM,\,Rep}$, red) and attractive ($F_{EM,Att}$, green). To intuitively represent the magnet's equilibrium position, we plotted the negative elastic force ($-F_{ES}$), generated by the stretched membrane, instead of the positive elastic force (F_{ES}) (Supplementary Fig. 2c). The elastic membrane resists the magnet's motion toward the electromagnet and vice versa. The intersections of these force curves, indicated by the black circles at t_0 and t_2, represent equilibrium points where the forces balance. Thus, the magnet in the NC-EsMV system oscillates between these positions. Here, the inertial effects are considered negligible. Consequently, the magnet's equilibrium points shift over time. The measured forces closely match the theoretical predictions (detailed in Supplementary Notes 1), validating our model for the dynamic force interactions in the system.

In C-EsMV system, at $t = t_0$, the magnet reaches its maximum displacement due to repulsion, and at $t = t_2$, it touches the electromagnet's surface because of the attractive forces, as shown in Supplementary Fig. 2d. Although the elastic force (F_{ES}) remains the same, but the magnet-magnet interaction force is added to the previous electromagnetic components ($F_{MM} + F_{EM,\,Rep}$ and $F_{MM} + F_{EM,\,Att}$) in Supplementary Fig. 2e. Optimal motion amplification occurs when the negative elastic force curve ($-F_{ES}$) is located between the maximum attraction ($F_{MM} + F_{EM,\,Att}$) and repulsion ($F_{MM} + F_{EM,\,Rep}$) curves. When $|-F_{ES}| < |F_{MM} + F_{EM,\,Att}|$ at t_2, the magnets collapse onto the electromagnet in the middle. As time progresses and $|-F_{ES}| > |F_{MM} + F_{EM,\,Att}|_{z=0}$ dominates at t_0, the magnet moves back to the balance point. However, due to significant inertia, static analysis alone is insufficient to fully capture the system's behavior. Static analysis inherently assumes equilibrium conditions without considering temporal effects, neglecting events preceding or following the equilibrium state. Thus, a dynamic analysis that explicitly incorporates acceleration and temporal context becomes essential. This dynamic perspective is discussed in detail in Fig. 2.

Supplementary Note 3. Resonant frequency in our system

In our system, the observed resonance corresponds to the nonlinear forced resonance of the coupled magnet–membrane system rather than the intrinsic free-vibration frequency. Consequently, the response around resonance is asymmetric: the vibration amplitude increases gradually as the frequency approaches resonance, but exhibits an eventual decay beyond the resonance frequency. At lower frequencies, the system surpasses the threshold to generate amplified vibration, and as the frequency approaches resonance, this effect further enhances the amplitude. Beyond resonance, however, the increasing phase mismatch between the magnet motion and the input signal reduces effective acceleration, preventing the system from overcoming the threshold and leading to weakened vibration and eventual decay.

This asymmetry primarily arises from the phase mismatch–induced loss of energy transfer efficiency at higher frequencies. In addition, the strongly nonlinear magnetic force, which intensifies as the inter-magnet distance decreases, further enhances this asymmetric response. Together, these effects cause the frequency response to deviate from the symmetric Lorentz-type profile typical of linear oscillators.

The intrinsic baseline frequency of the magnet–membrane pair, in the absence of magnetic and damping forces, can be approximated by the mass–spring relation:

$$\omega_0 = \sqrt{\frac{k_{\mathrm{ES}}}{m}} \tag{9}$$

where k_{ES} is the spring constant of membrane and m is the magnet–membrane mass.

When magnetic and damping forces are included, the system can be linearized locally around an equilibrium position z^*:

$$\begin{aligned} m\,z'' + c_{\mathbf{ef}}\,z' + k_{\mathbf{ef}}\,z &= 0, \\ k_{\mathbf{ef}} &= \frac{\delta(F_{\mathrm{ES}} - F_{\mathrm{M\,M}})}{\delta z}_{\mathrm{at\ z=z^*}}, \end{aligned} \tag{10}$$

The corresponding damped frequency is given by:

$$\omega_{\mathrm{d}} = \sqrt{\frac{k_{\mathbf{ef}}\,(z^*)}{m} - \left(\frac{c_{\mathbf{ef}}}{2m}\right)^2}, \tag{11}$$

where c_{eff} denotes the effective damping coefficient of the membrane, which in our system may depend not only on velocity but also on displacement due to the viscoelastic membrane behavior and contact conditions. k_{eff} (z^*) varies dynamically with the equilibrium position determined by the applied magnetic forces. Thus, the resonant frequency shifts continuously with both equilibrium position and input current, confirming that the observed resonance arises from a nonlinear forced response rather than a fixed natural frequency.

For small oscillations around an equilibrium z^*, $c(z)$ can be approximated as constant, yielding a well-defined local damped natural frequency. However, in the amplified state, the C-EsMV traverses both equilibria with large excursions, where the restoring and damping forces vary significantly within each cycle. The motion is therefore better described as a nonlinear forced periodic response (limit cycle) governed by the AC electromagnetic drive, whose magnitude depends on displacement while its temporal variation follows the input frequency. This displacement dependence introduces nonlinear stiffness effects, broadening and shifting the resonance relative to eq. (9).

Although the membrane can, in principle, support multiple vibration modes, our experiments operated near the fundamental resonance, where phase mismatch and potential damping effect of membrane strongly suppresses higher-order responses. Weak secondary resonances may appear under certain conditions but are highly sensitive to asymmetry and nonlinear coupling. If geometric or material asymmetry were introduced, multimode or non-axisymmetric oscillations could emerge, leading to richer nonlinear dynamics under modified designs or excitation conditions.

Supplementary Note 4. Design map for optimal region

In extension to Fig. 3a, we further examined the system by analyzing combinations of characteristic magnetic and elastic forces from various perspectives. As shown in Supplementary Fig. 7a, the system enters an *amplified* state (highlighted in yellow) when the membrane force and magnetic force are balanced. However, the range over which amplification occurs (amplifiable range, ΔD) varies under different cases (Supplementary Fig. 7b). The *weakened* state (indicated in blue) dominates when the magnetic force is disproportionately large or small, regardless of the membrane's initial position (D). The maximum amplitude achievable by the system occurs at the optimal initial position (D_{opt}), placed at the boundary between the *amplified* state (or the *collapsed* state, if amplification is not possible) and the *weakened* state.

Supplementary Fig. 7c demonstrates that the D_{opt} increases as the membrane force (F^*_{ES}) decreases and the magnetic force (F^*_{MM}) increases, indicating that stronger magnets can initiate amplification from farther distances by more easily overcoming the membrane's restoring force. Supplementary Fig. 7d and e further show that, at the optimal position (D_{opt}) of each force combination (F^*_{ES}, F^*_{MM}), high velocity and acceleration are observed along an upward-sloping amplification boundary where the elastic and magnetic forces are in balance. Among the systems capable of amplification, those with weaker elastic forces tend to exhibit even higher velocities and accelerations. This is because stronger, less stretchable membranes more severely restrict the magnet's displacement, thereby limiting its dynamic motion.

Moreover, increasing the magnetic force often requires larger magnets, as magnetic materials have finite magnetization. While this increases the magnetic force, it also raises the system's mass, which could reduce acceleration. Nevertheless, as shown in Supplementary Fig. 7f, systems with greater magnetic forces—and consequently larger masses—generally exhibit higher kinetic energies.

Table 2. Characteristic parameters and forces for four cases

Case	Membrane modulus (kPa)	Magnet thickness (mm)	F^*_{ES} (N)	F^*_{MM} (N)
I	50	0.5	0.2419	0.0348
II	50	1.5	0.2419	0.2072
III	110	1.5	0.6289	0.2072
IV*	80	2.2	0.3870	0.3463

All other parameters remain unchanged. *Simulated

Supplementary Note 5. Characterization of C-EsMV based on the initial magnet position, *D*.

The C-EsMV can exhibit three distinct states—*collapsed*, *amplified*, and *weakened*—based on the relative positions of the magnets, electromagnet, and membrane. We numerically analyzed these states by fixing all parameters except the initial magnet position (D) relative to the electromagnet surface (Supplementary Fig. 9a). Adjusting D shifts the membrane's equilibrium position, shown in parallel displacements of the membrane force F_{ES} along the x-axis (from ① to ④ in Supplementary Fig. 9b).

In the *collapsed* state (region including ①), the membrane is so close to the electromagnet that the combined force of magnet attraction and maximum electromagnet repulsion ($F_{MM} + F_{EM,\,Rep,}$ red line) exceeds the elastic force of membrane at the bottom surface. When $|F_{ES}(z = 0)| < |F_{MM}(z = 0) + F_{EM,\,Rep}(z = 0)|$, the magnet remains attached and cannot detach, indicating a *collapsed* configuration.

In the *amplified* state (region including ②), the membrane force curve $-F_{ES}$ lies between the repulsive and attractive force curves (red and green lines). In this regime, $-F_{ES} > F_{MM} + F_{EM,\,Att}$ for all z, and $|F_{ES}(z = 0)| > |F_{MM}(z = 0) + F_{EM,\,Rep}(z = 0)|$, leading to a greatly amplified stroke between the bottom surface and the upper equilibrium position.

In the *weakened* state (regions including ③ and ④), the membrane force curve, $-F_{ES}$, is below $F_{MM} + F_{EM,\,Att}$ for some point ($\exists\, z$ such that $-F_{ES} < F_{MM} + F_{EM,\,Att}$), meaning the magnet is not sufficiently displaced toward the bottom, and the system fails to reach the amplified stroke.

The *weakened* state can be further subdivided into *shootable* (area including ③) and *non-shootable* (area including ④) regimes, based on whether the actuator can be externally triggered into the amplified state. In the *shootable* regime, the condition $-F_{ES} > F_{MM} + F_{EM,\,Att}$ creates an energy barrier. However, amplification can still occur by manually bringing the magnets into contact with the electromagnet at least once. The initial attachment allows the system to sustain amplification via magnet's inertia, which helps overcome the energy barrier in subsequent cycles.

In contrast, the *non-shootable weakened* state occurs when the membrane is too far from the electromagnet. Here, the magnetic attraction and maximum repulsion are both weaker than the membrane force at $z = 0$ ($|F_{ES}| < |F_{MM} +$

$F_{EM, Rep}$|), preventing any contact between the magnet and electromagnet. As a result, the system experiences damped vibrations and cannot initiate amplification. This highlights the importance of dynamic analysis, as static force conditions alone do not capture the possibility of induced motion.

The total force and energy profiles in Supplementary Fig. 9c-f illustrate the key characteristics of each state at representative D values (2.5, 3.9, 4.5, 8.0 mm) during both attractive and repulsive phases. In the *collapsed* state, the energy barrier persists throughout both phases, preventing detachment from $z = 0$ (Supplementary Fig. 9c). In the *amplified* state, this barrier vanishes, and energy landscapes near the bottom are monotonic in both phases, enabling alternating attachment and detachment (Supplementary Fig. 9d). In the *shootable weakened* state, the energy barrier during the attractive phase indicates the minimum trigger energy required for amplification (Supplementary Fig. 9e). The corresponding force profile shows the minimum trigger force and the maximum bearable load, defined as the heaviest object the C-EsMV system can support without losing its amplification capability. Lastly, in the *non-shootable weakened* state, the energy barrier is absent in both phases, producing a profile similar to that of NC-EsMV (Supplementary Fig. 9f).

Supplementary Note 6. Efficiency of the system

To evaluate the performance of the C-EsMV system, we compare the efficiency under various input waveforms relative to that under a sinusoidal input. The absolute efficiency is defined as the ratio of output kinetic energy to input electrical energy and it is relatively low (~1%) when driven by sinusoidal currents through electromagnets. However, this value is not fixed; rather, it can be substantially enhanced from two perspectives.

First, the magnetic field generated by the electromagnet is given by $B = \mu n i$, where n is the number of coil turns and i is the current. The current low efficiency of the C-EsMV system is primarily attributed to the use of a small and lightweight electromagnet (1 g, 40 turns), which necessitates a high driving current. Efficiency can be improved by increasing the number of the coil turns (n), thereby reducing the required current and, thus, the input electrical energy. Since this system is intended for stationary applications, where weight is not a limiting factor, this trade-off would be acceptable for practical scenarios. Crucially, high current itself does not benefit the system; rather, amplification is triggered once a threshold current is surpassed. Lowering this threshold allows the system to operate at lower input currents, thereby enhancing overall efficiency and broadening its application potential.

The second approach involves maintaining the same peak current required for amplification while modifying the input wave form, as shown in Fig. 3i. Since electrical energy input corresponds to the time-integral for voltage (or current), minimizing the area under the input signal while still reaching the amplification threshold significantly improves efficiency. We demonstrate that using a pseudo-Gaussian waveform, with the same electromagnet and peak current, achieves amplification with a 64-fold increase in efficiency compared to a sinusoidal input. Further optimization of the waveform to achieve smaller integral area with a sharp, brief peak could improve efficiency even more.

Optimizing either the electromagnet structure or the input waveform presents a promising route for enhancing the absolute efficiency of the C-EsMV system. Nonetheless, the primary contribution of this study is to demonstrate that meaningful motion amplification can be achieved by balancing magnet-magnet interaction through elastic energy. We further envision that the electromagnet could be replaced with alternative actuation methods, such as electrical or pneumatic actuators, that can similarly balance two key forces (F_{MM}, and F_{ES}) for improved adaptability and energy performance. While these engineering refinements are important, the present work focuses on establishing the fundamental principle underlying elastic-mediated magnetic amplification.

Supplementary Figure:

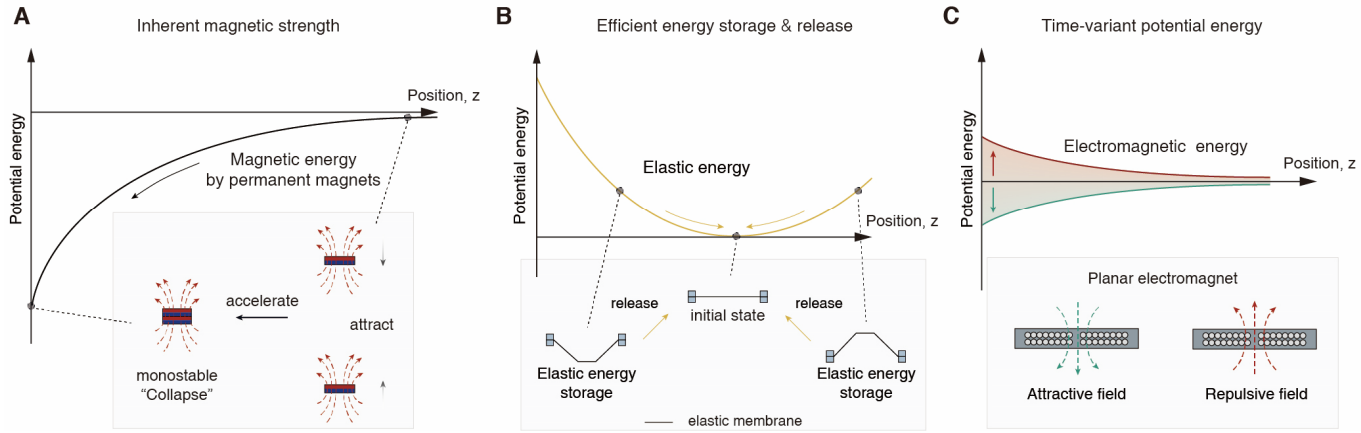

Supplementary Fig. 1. Schematic representation of potential energy in (a) attractively coupled magnets, (b) an elastic membrane, and (c) an electromagnet.

In (a), two like-pole magnets accelerate toward each other until they collapse into a stable configuration (black line), reflecting their inherent magnetic strength. In (b), the introduction of an elastic membrane allows the magnetic collapse to be controlled, with the membrane efficiently storing and releasing energy as elastic potential energy. In (c), a planar electromagnet generating an alternating magnetic field enables the creation of a dynamic system with tunable instability.

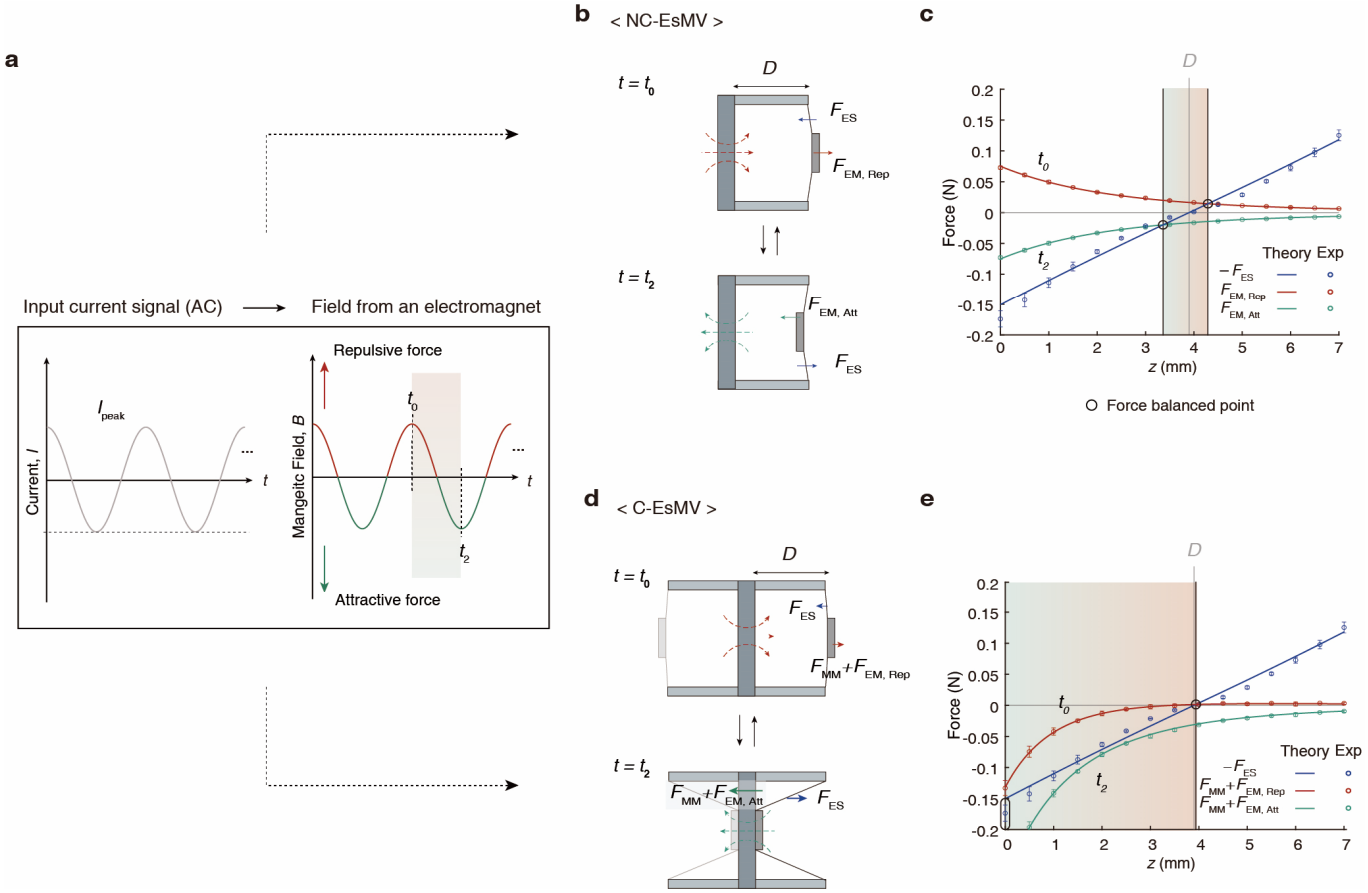

Supplementary Fig. 2. Static force analysis of non-coupled (NC-EsMV) and coupled (C-EsMV) systems.

(a) Input current applied to the electromagnet and the resulting magnetic field generated. (b) The position of the magnet during vibration at $t = t_0$ and $t = t_2$ in NC-EsMV system. (c) A static force diagram showing the individual forces acting on the magnet, including the elastic force (F_{ES}) and electromagnetic forces ($F_{EM, Att}$ and $F_{EM, Rep}$). In the NC-EsMV system, the magnet oscillates between two force balance points, with the inertial effect considered negligible. (d) The position of the magnet during vibration at $t = t_0$ and $t = t_2$ in C-EsMV. (e) Static force diagram for C-EsMV system, where the magnetic forces are plotted as the sum of the electromagnetic components ($F_{MM} + F_{EM, Rep}$ and $F_{MM} + F_{EM, Att}$). While the static analysis shows the magnet oscillating between two balance points, the significant inertia in the system requires a dynamic analysis for a more accurate interpretation, which is detailed in Fig. 2. Error bars denote SDs; n = 3.

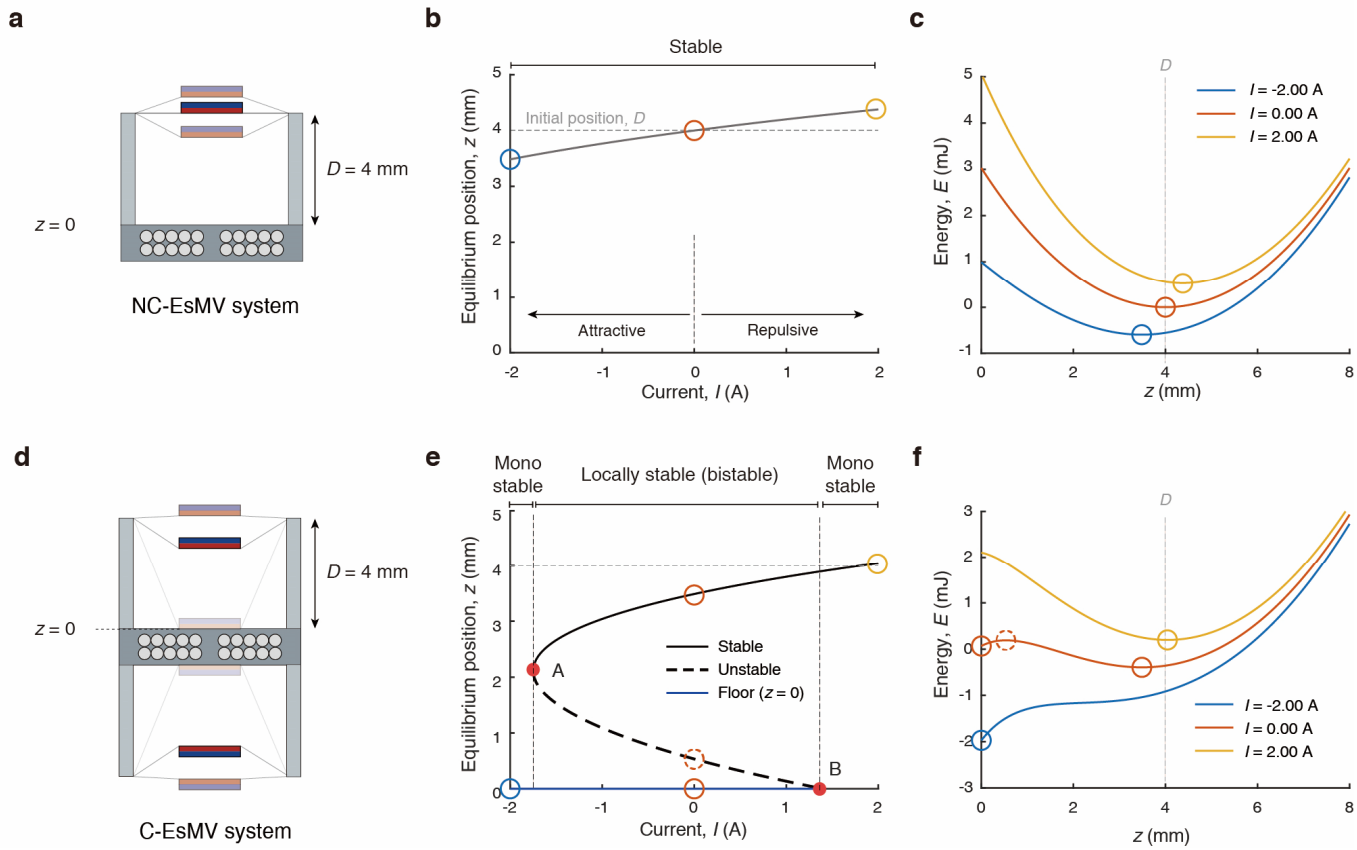

Supplementary Fig. 3. Static analysis of equilibrium and energy as current is varied.

(a) Schematic of the NC-EsMV with variable current (*I*). (b) State diagram showing equilibrium positions of the NC-EsMV system as a function of input current. (c) Energy landscape of the NC-EsMV system plotted as a function of position for different input currents (−2, 0, and 2 A). (d) Schematic of the C-EsMV. (e) State diagram showing equilibrium positions of the C-EsMV system as a function of input current. (f) Energy landscape of the C-EsMV system plotted as a function of position for different input currents (−2, 0, and 2 A) (Point A: Saddle-node fold, Point B: Subcritical Hopf).

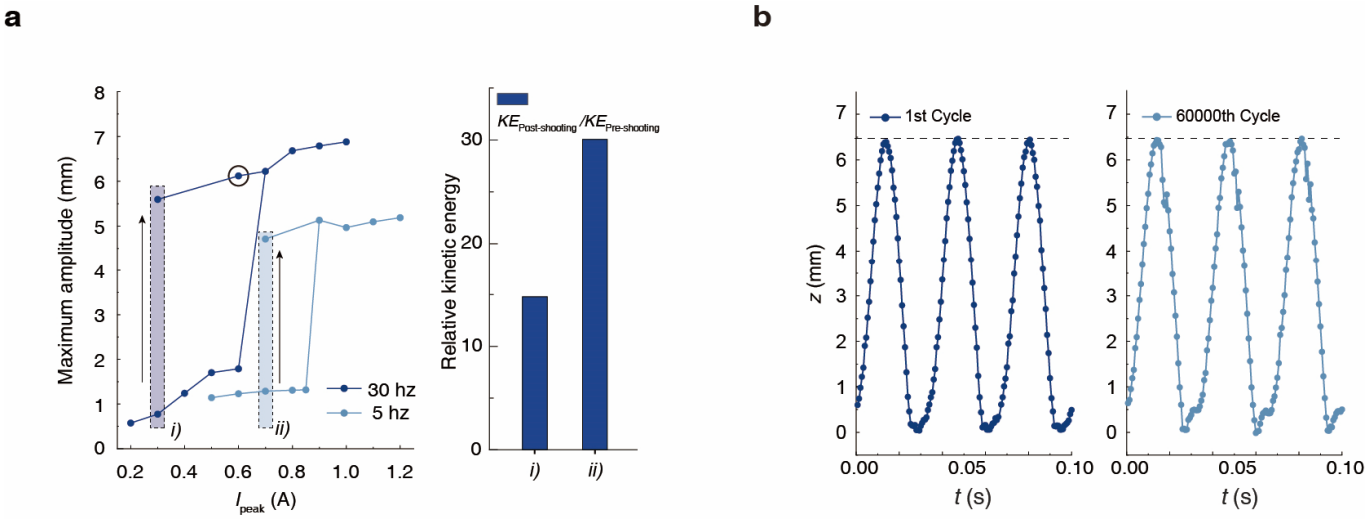

Supplementary Fig. 4. Energy conversion efficiency and cyclic stability of vibrational hysteresis.

From the vibrational hysteresis shown in Fig. 1g, two key properties are measured. (a) The ratio of kinetic energy of the shooted mode to that of non-shooted mode was evaluated for each condition in C-EsMV system: (i) 0.3 A at 30 Hz and (ii) 0.7 A at 5 Hz. The energy gain with and without shooting was assessed, showing a significant increase when shooting is utilized. (b) Cyclic stability of shooting at 0.6 A and 30 Hz. Even after 60,000 cycles, stable behavior was observed, demonstrating the system's robust cyclic stability.

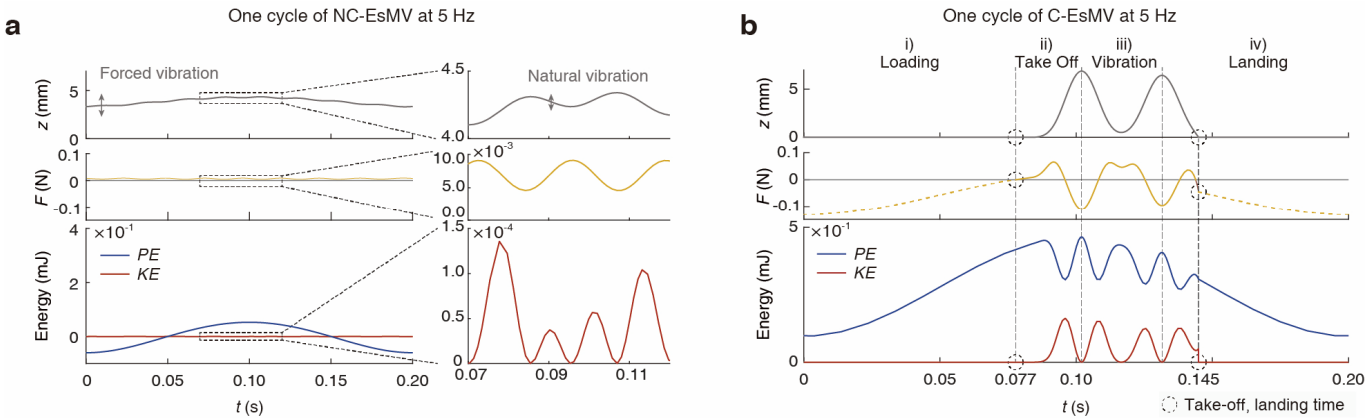

Supplementary Fig. 5. Numerical results for magnet's position (*z*), net force (*F*), and potential and kinetic energies during a single actuation cycle of (a) NC-EsMV and (b) C-EsMV at f_i = 5 Hz.

Key moments, such as *take-off* and *landing*, are highlighted with dashed circles, and dashed curves are used in the force plot to indicate the zero-net-force regimes. *i) loading, ii) take-off, iii) vibration,* and *iv) landing*, marked by vertical dashed lines. Initially, the magnet collapses onto the electromagnet's surface, storing maximum elastic potential energy (*i*, 0 s < t < 0.077 s). When electromagnetic repulsion increases sufficiently to yield a net positive force, it triggers the *take-off* (*ii*, t = 0.077 s). After *take-off*, the system enters a vibration phase governed by its natural frequency (*iii*, 0.102 s < t < 0.132 s), then returns to the electromagnet's surface to complete the cycle (*iv*, 0.132 s ≤ t ≤ 0.2 s).

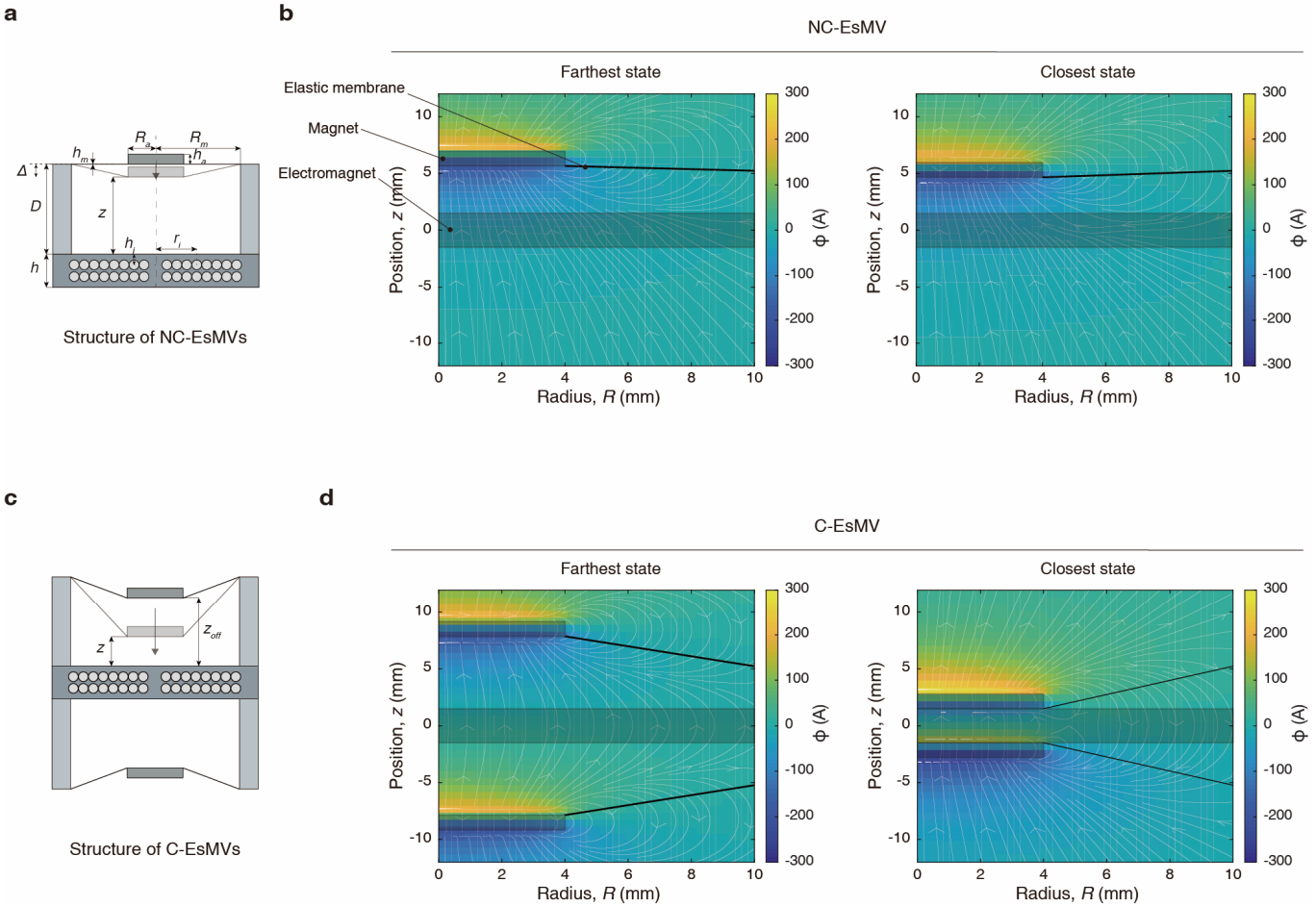

Supplementary Fig. 6. Structural parameters and magnetic scalar potential in the farthest and closest positions of the magnet from the electromagnet phases, for (a and b) NC-EsMV and (c and d) C-EsMV systems.

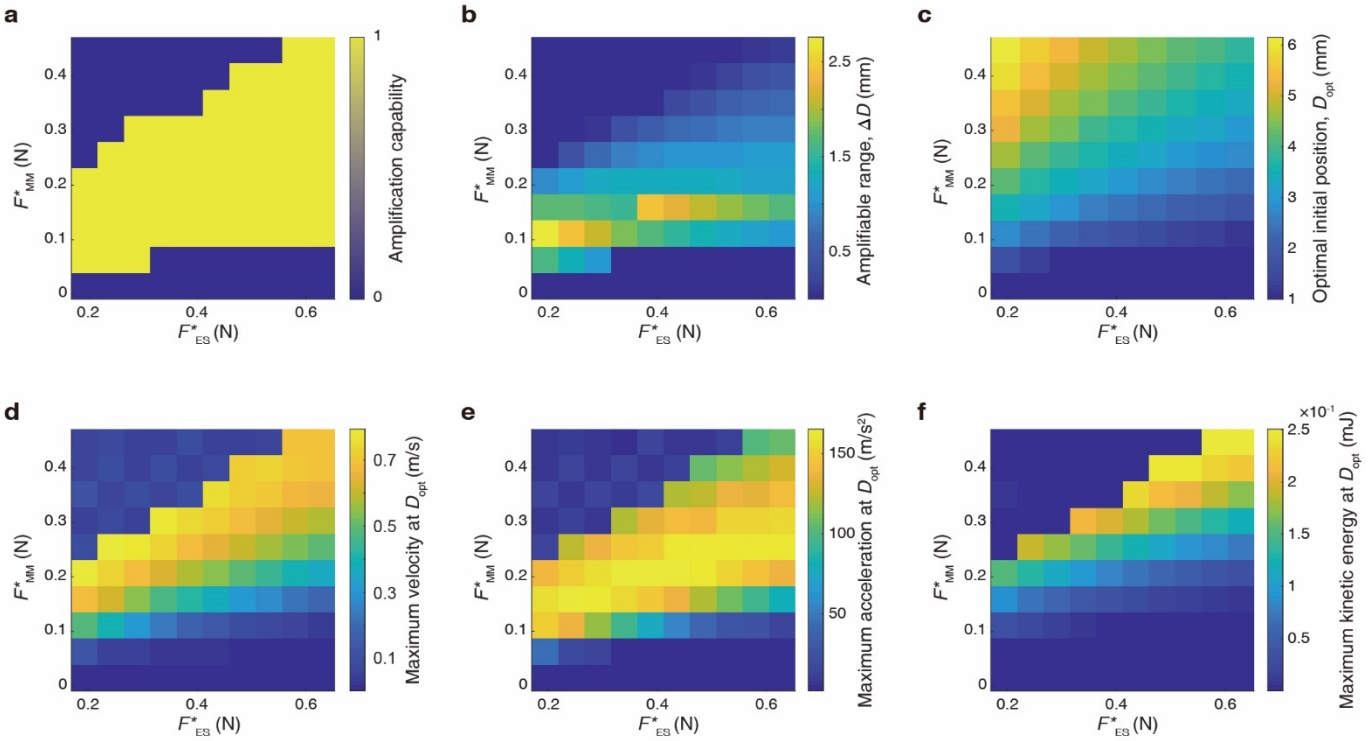

Supplementary Fig. 7. Design map for different cases with varying elastic and magnetic forces. (I_{peak} = 2.0 A)

(a) Amplification capability (yellow: amplifiable, blue: non-amplifiable), (b) range of amplifiable initial positions (D), (c) optimal initial position (D_{opt}), (d) maximum velocity, (e) maximum acceleration, (f) maximum kinetic energy of C-EsMV plotted against characteristic values F^*_{ES} and F^*_{MM}.

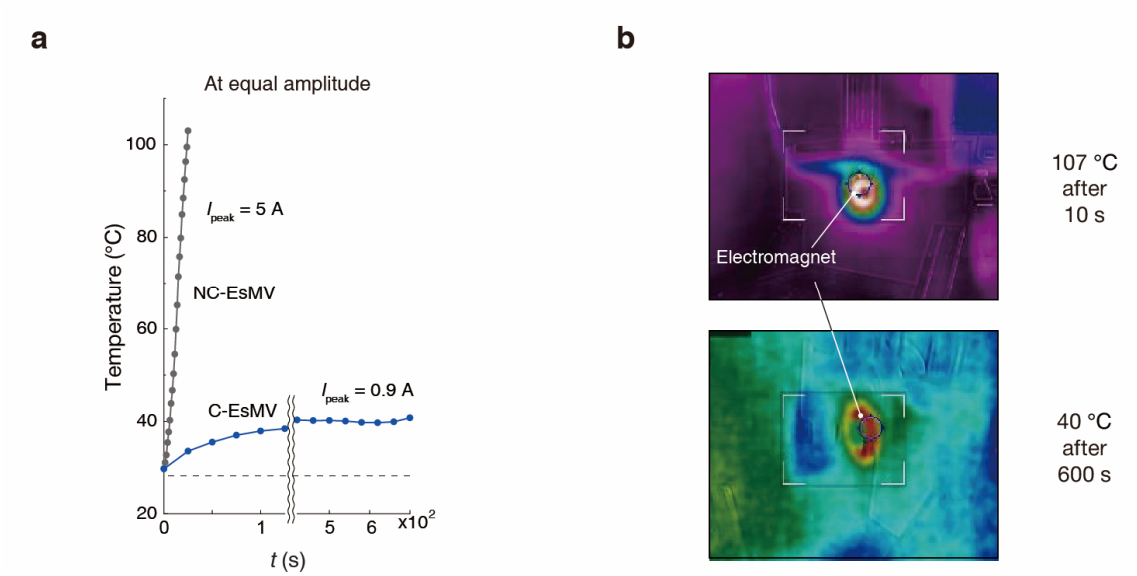

Supplementary Fig. 8. Comparison of thermal stability for each system.

A thermocouple attached to the surface of the electromagnet was used to monitor the real-time temperature during the operation of both NC-EsMV and C-EsMV. (a) For equal amplitude vibrations (D = 2.5 mm), the temperature in NC-EsMV rises exponentially from room temperature to 107 °C within 10 s, while in C-EsMV, the temperature stabilizes at 40 °C, even after 600 s of vibration, demonstrating superior thermal stability due to higher energy efficiency compared to NC-EsMV. (b) Infrared camera images showing the temperature distribution for each case.

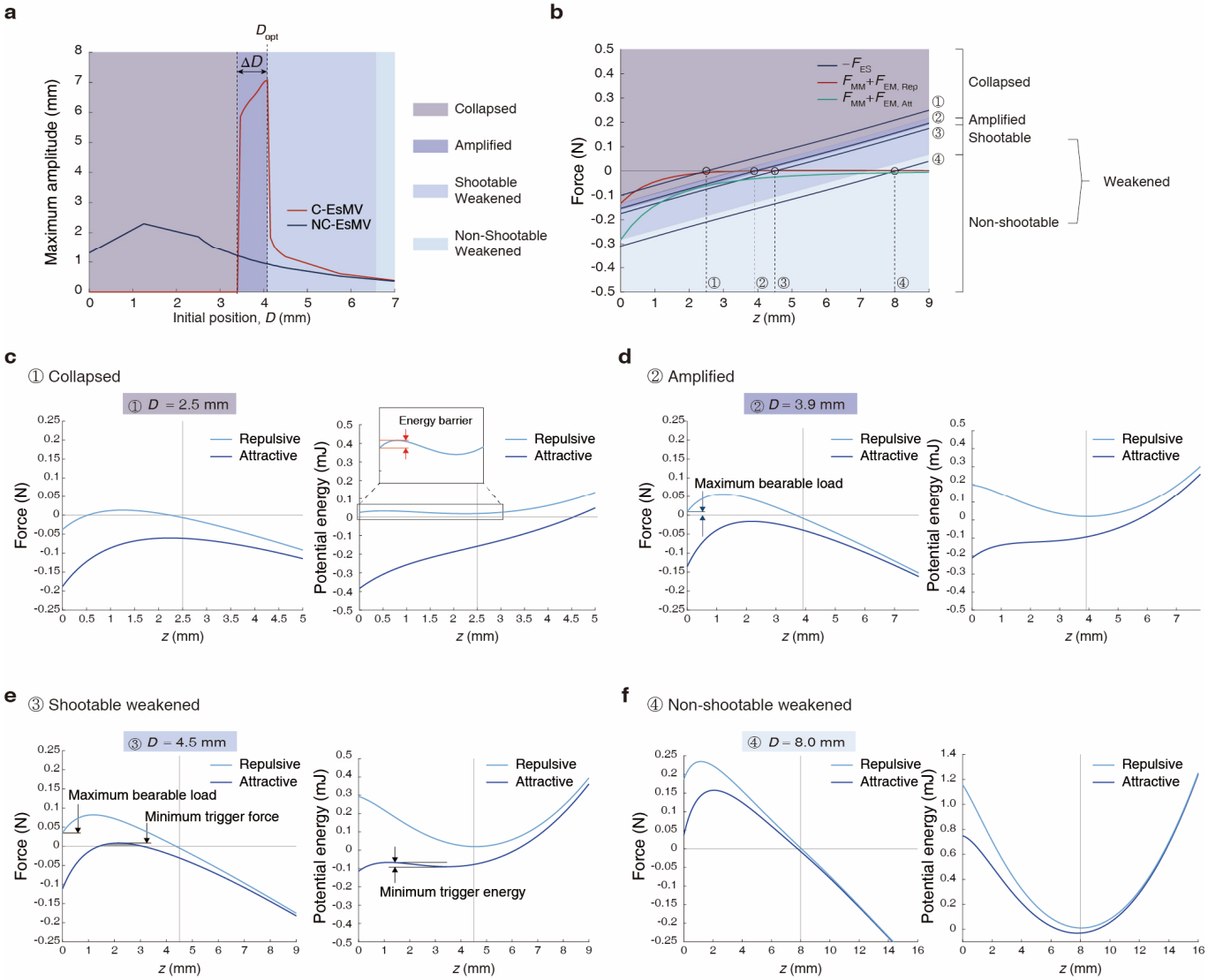

Supplementary Fig. 9. Characterization of C-EsMV based on the initial position *D*.

(a) Initial position-amplitude plot and (b) displacement-force plot of a C-EsMV across varying initial positions, divided into four different regimes. The total force and energy by position for each regime, (c) collapsed, (d) amplified, (e) shootable weakened, and (f) non-shootable weakened highlights the behavior of C-EsMV under various scenarios.

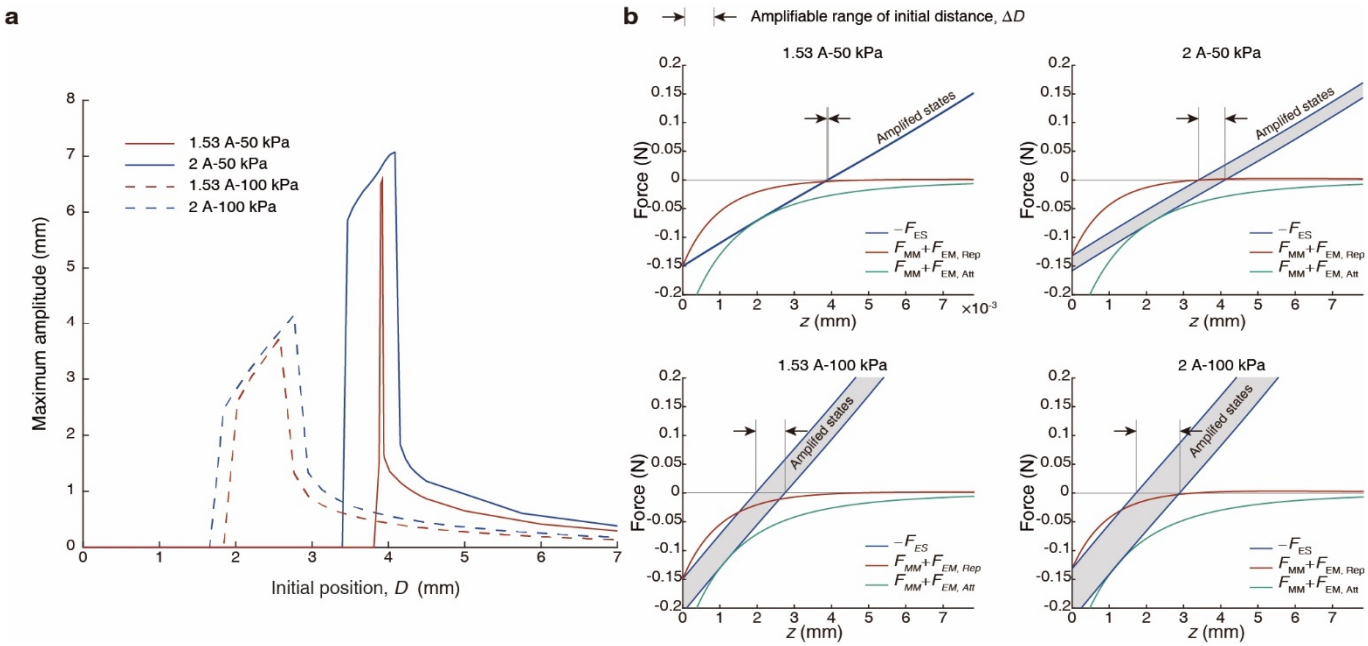

Supplementary Fig. 10. Comparison of four different C-EsMV systems with varied current (I_{peak} = 1.53, 2 A) and membrane modulus (E = 50, 100 kPa) conditions.

(a) Initial position-amplitude and (b) displacement-force plot of the four systems. The shaded area indicates the range of positions where amplification is possible. A higher electric current and a higher elastic modulus expand the amplification range, while a stronger membrane force results in the magnet being positioned closer to the electromagnet.

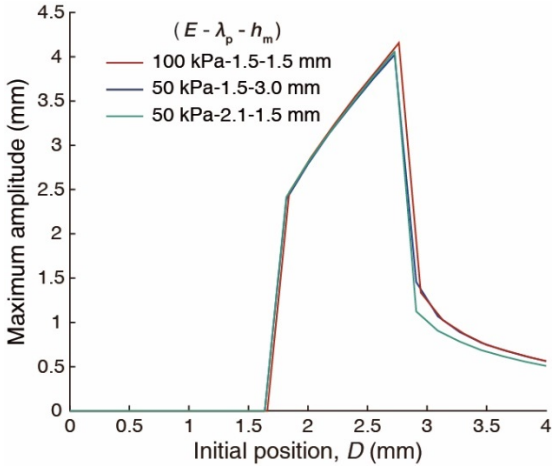

Supplementary Fig. 11. Initial position-amplitude plot of C-EsMV system with varying conditions of elastic membrane, but with identical characteristic membrane force F^*_{ES}.

The three elastic membranes are each specified by different combinations of Young's Modulus E (kPa), prestretch λ_p, and final membrane thickness h_m (mm): (100, 1.5, 1.5), (50, 1.5, 3.0), and (50, 2.1, 1.5). These configurations ensure a consistent characteristic force, $F^*_{ES} = 0.49$ (N). When F^*_{ES} remains unchanged, the C-EsMV demonstrate similar performance outcomes, highlighting the system's scalability despite variations in membrane physical properties. Any slight deviations observed are due to the nonlinear higher-order effects of the membrane force and the damping force.

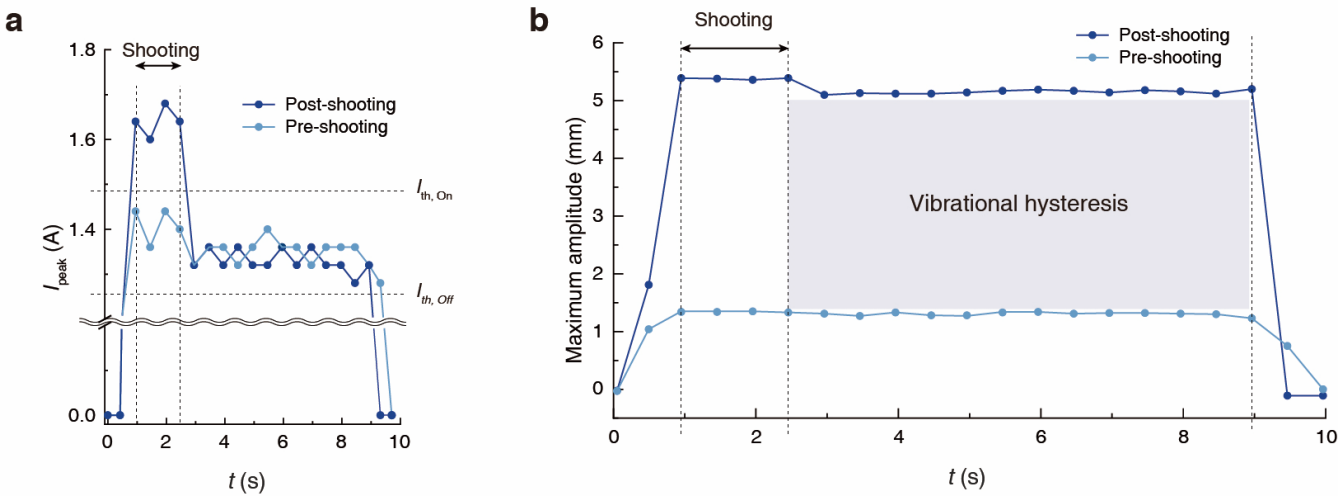

Supplementary Fig. 12. Experimental verification of vibrational hysteresis in C-EsMV.

(a) Input current signal for the two cases: pre-shooting (I_{peak} ~ 1.4 A) and post-shooting (I_{peak} ~ 1.4 → 1.6 A → 1.4 A). (b) Maximum amplitude for each case. When using shooting mechanism, even when the signal returns to the original peak current, the amplification is maintained. The shaded area represents energy saved through vibrational hysteresis, facilitated by inertia during shooting.

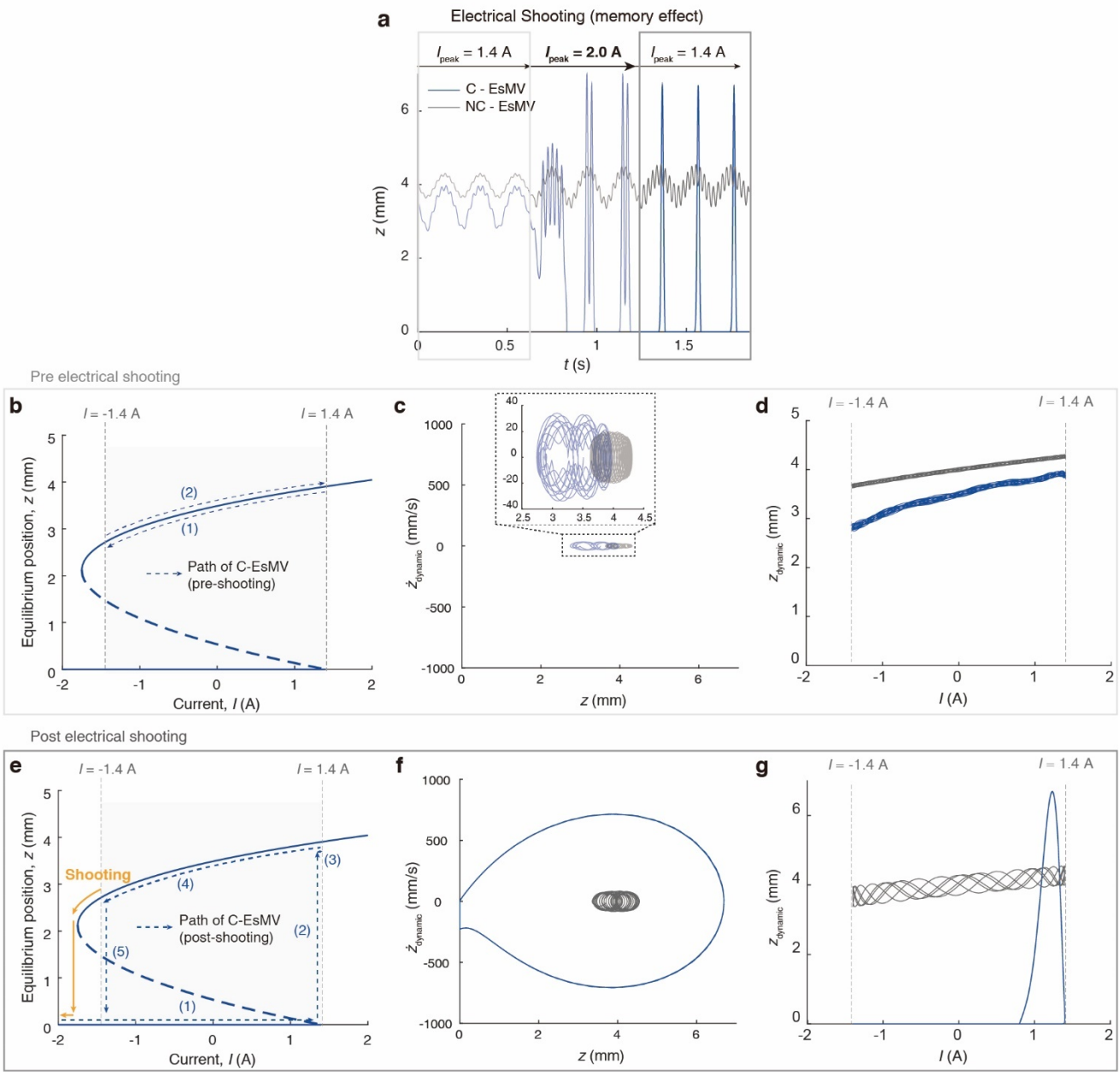

Supplementary Fig. 13. Numerical results of electrical shooting behavior and motion hysteresis in C-EsMV.

(a) Vibration motion of NC-EsMV and C-EsMV at a driving frequency of 5 Hz (D = 4.0 mm). Even after the current is increased from 1.4 A to 2.0 A and then returned to 1.4 A, the amplified vibration of C-EsMV is maintained. The shooting process enables C-EsMV to reach the amplified mode at lower currents that were previously unattainable, as clearly seen in the phase portraits. (b–d) Static and dynamic vibration paths at I_{peak} = 1.4 A before shooting: (b) Bifurcation diagram of C-EsMV showing equilibrium positions, (c) corresponding phase portraits of C-EsMV and NC-EsMV, and (d) dynamic vibration trajectory under sinusoidal electrical input, which closely follows the equilibrium path. (e–g) Static and dynamic vibration paths at I_{peak} = 1.4 A after shooting: (e) Bifurcation diagram of C-EsMV showing a switched branch after shooting, (f) phase portraits of C-EsMV and NC-EsMV, and (g) dynamic vibration trajectory under repeated sinusoidal input, exhibiting significantly larger oscillations despite the same current amplitude.

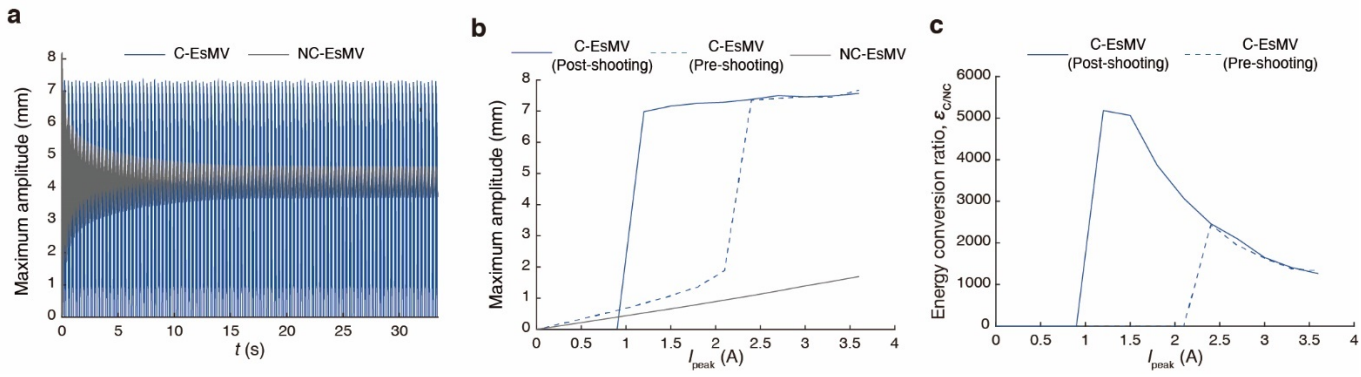

Supplementary Fig. 14. Stability and efficient energy conversion after shooting.

(a) Temporal evolution of NC-EsMV and C-EsMV after the initial shooting (D = 4.2 mm). The vibration in NC-EsMV system quickly decays due to internal damping, while amplification in C-EsMV persists over time. (e) Maximum amplitude and (f) coupling-to-non-coupling energy conversion ratio ($\varepsilon_{\mathrm{C/NC}}$) as a function of input current for NC-EsMV and C-EsMV before and after shooting. The results demonstrate that C-EsMV achieves higher efficiency than NC-EsMV under the same low-current conditions, and that post-shooting operation further enhances efficiency compared to the pre-shooting state within the same C-EsMV system.

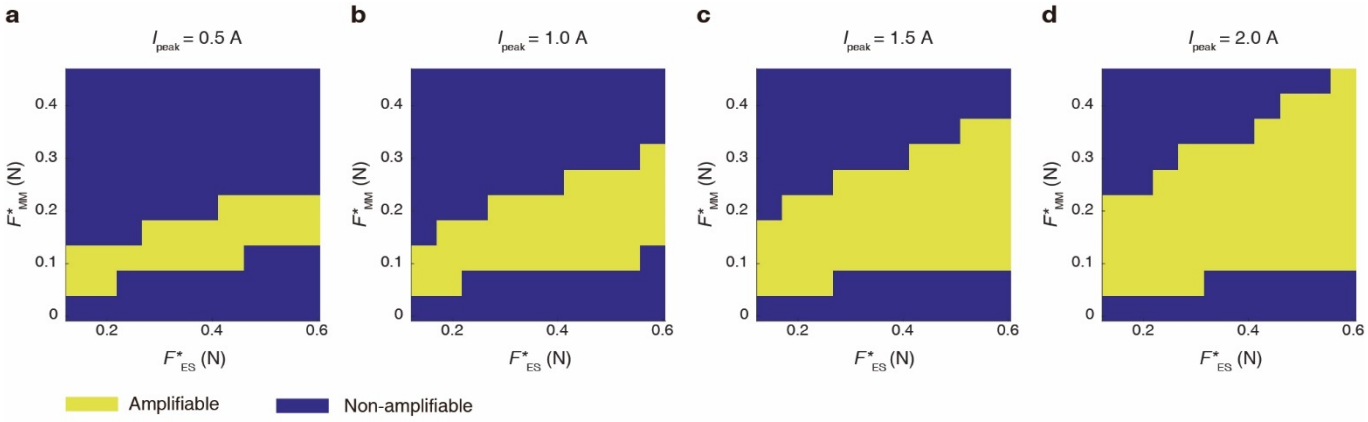

Supplementary Fig. 15. Change in amplifiable regions based on electromagnet input current at I_{peak} of (a) 0.5 A, (b) 1.0 A, (c) 1.5 A, and (d) 2.0 A.

As the current increases, both repulsive and attractive forces become stronger, enabling amplified vibrations over a wider range of magnetic-elastic force combinations.

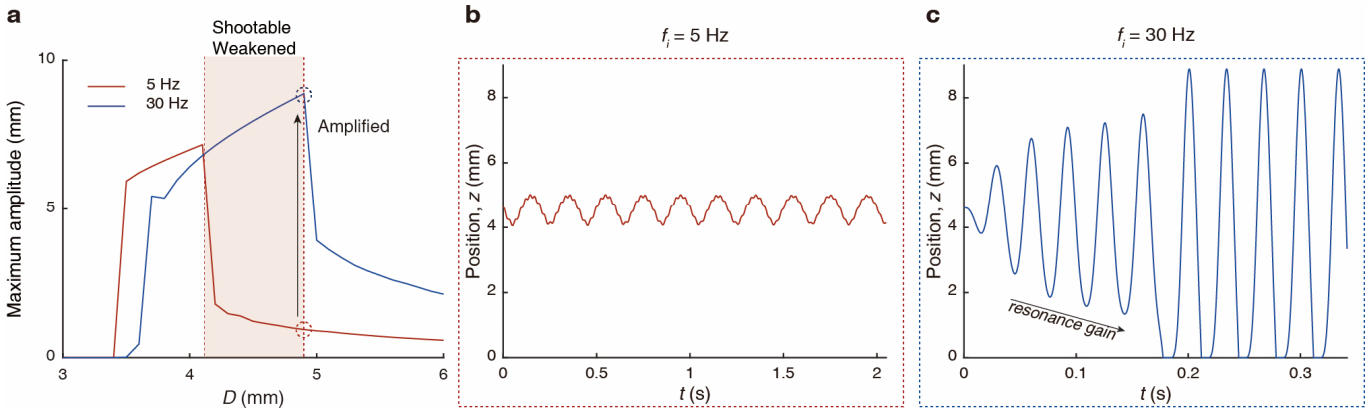

Supplementary Fig. 16. Vibration behavior in a C-EsMV system at different frequencies.

(a) Modulating input frequencies (f_i = 5 Hz to 30 Hz) extends the amplifiable range from the 'shootable weakened' regime to the 'amplified' regime. (b and c) Vibration of each C-EsMV system measured at the optimal distance, D_{opt}, at 5 and 30 Hz.

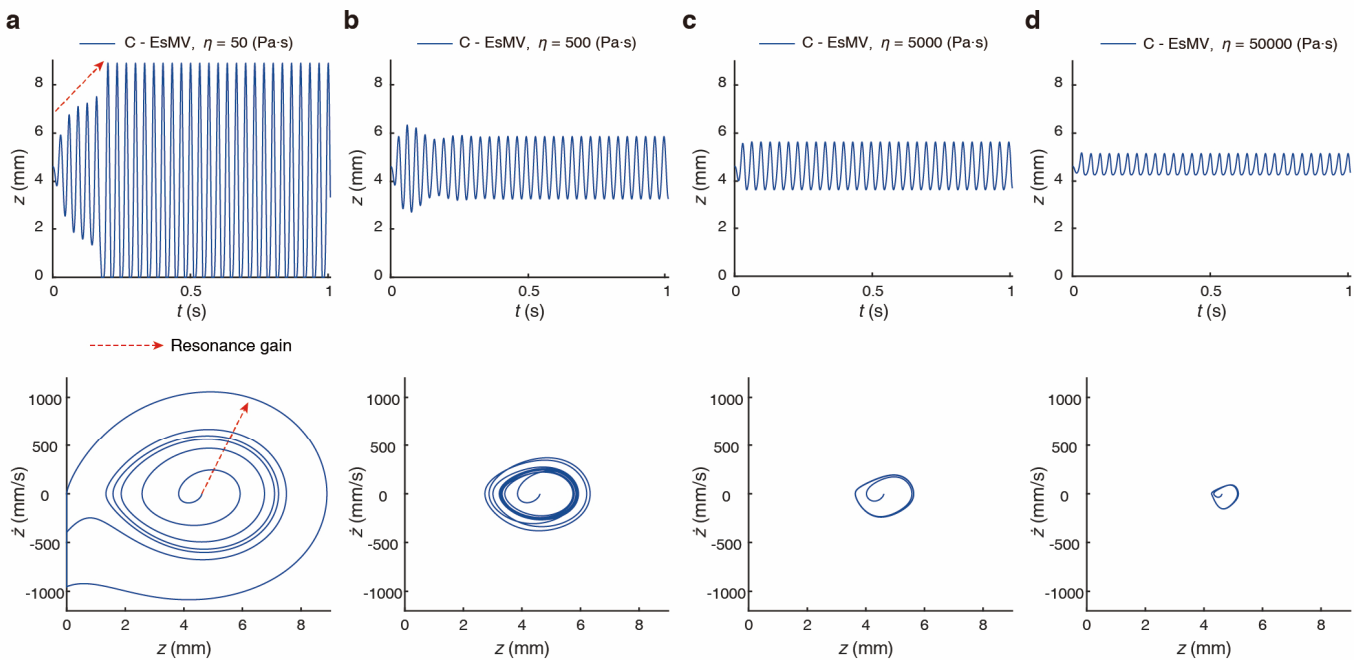

Supplementary Fig. 17. Time-resolved dynamic analysis of membrane motion under resonance at different dynamic viscosities.

(a-d) Dynamic responses when the input frequency is shifted from 5 Hz to 30 Hz, showing the effect of resonance gain at various viscosities: (a) η = 50 Pa·s, (b) η = 500 Pa·s, (c) η = 5000 Pa·s, and (d) η = 50,000 Pa·s.

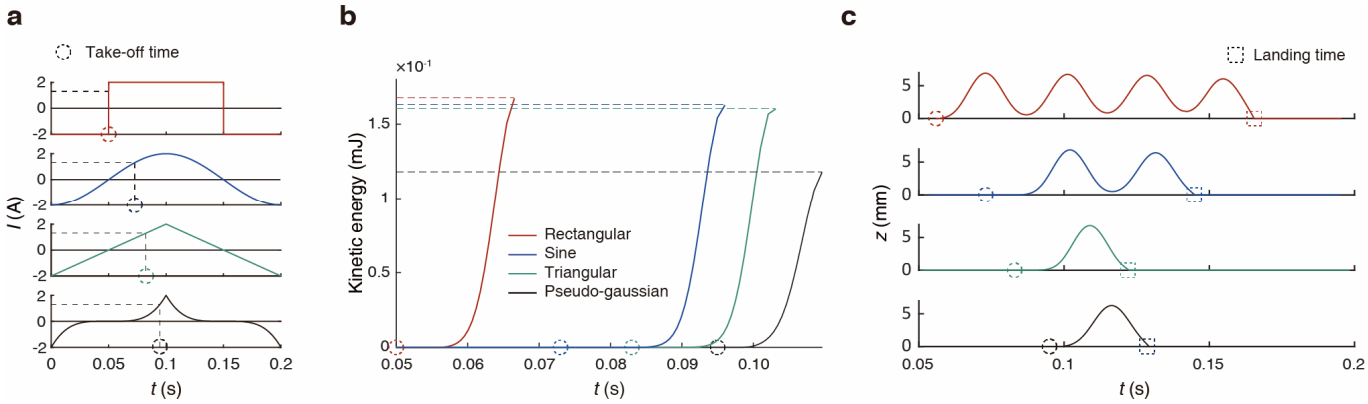

Supplementary Fig. 18. Vibration behavior in a C-EsMV system with different waveforms.

(a) Four types of waveforms: rectangular, sinusoidal, triangular, and pseudo-Gaussian are illustrated. Dotted circle marks the take-off moment of the magnet. (b) Kinetic energy over time during take-off. The rectangular waveform reaches the threshold current quickly, resulting in faster take-off. Differences in kinetic energy arise from varying input energies across waveforms. (c) Full cycle duration (from loading to landing) for each waveform. Both take-off and landing times differ depending on the waveform used.

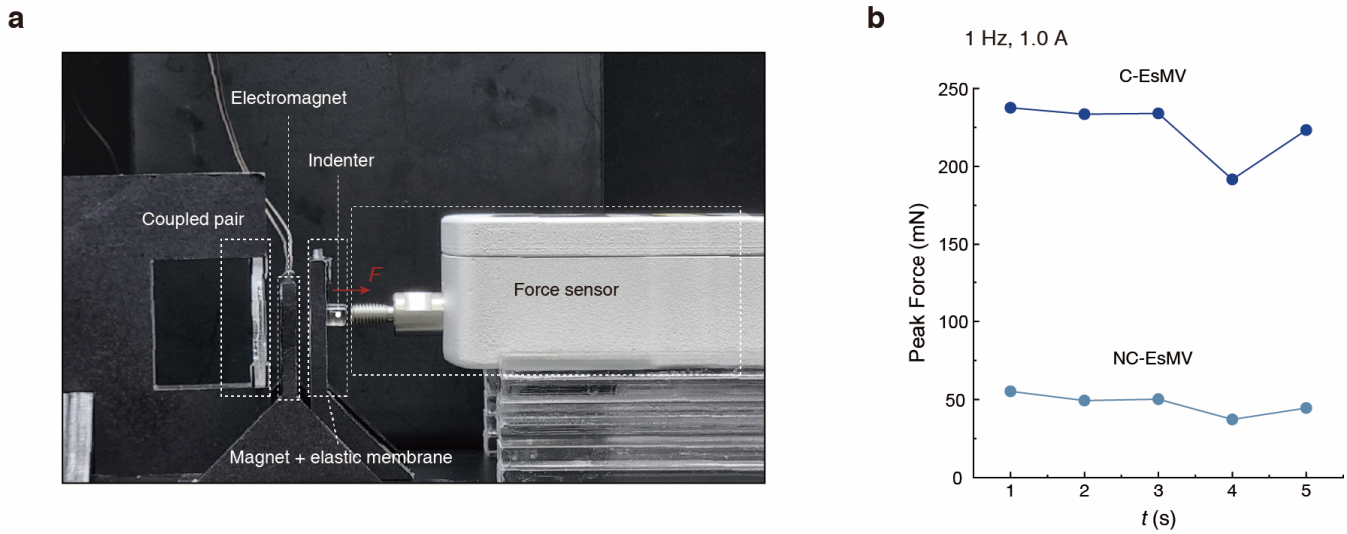

Supplementary Fig. 19. (a) Experimental setup for impact force measurement and (b) real-time peak force at 1 Hz.

A force meter (MARK-10, series 5) was used to measure the impact force during actuation. The system reaches its maximum velocity near the initial membrane position (*D*), where the membrane stretch is minimal. Therefore, the force sensor was positioned at *D* for the accurate measurement. Similarly, a thin glass wall (0.1 mm) was set at this position. The average value of five peak forces over time was used to represent the peak impact force.

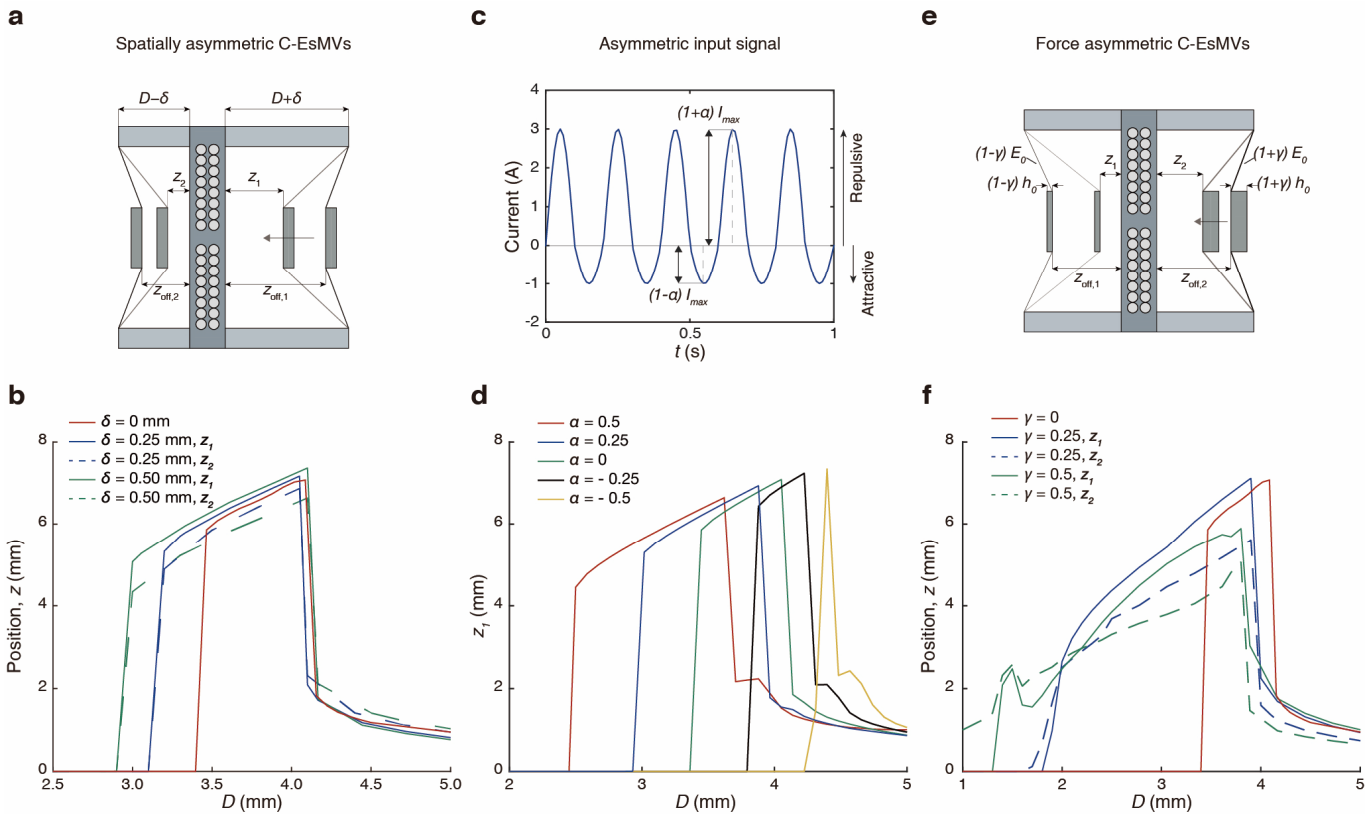

Supplementary Fig. 20. The effect of anisotropy on amplified vibration.

(a) Asymmetric structure and (b) its amplified motion as a function of distance when structural anisotropy is controlled by δ. As δ increases, one magnet moves closer to the electromagnet, making amplification easier and expanding the amplifiable region. The thicker spacer side (z_1) shows a larger amplitude.

(c) Asymmetric waveform input current and (d) its amplified motion as a function of distance when waveform anisotropy is controlled by α, which is defined as the percentage difference between the positive and negative peaks of the AC input: positive peak = (1+ α), negative peak = (1- α). A lower α (stronger attraction) allows amplification at greater distances, but narrows the amplifiable region after collapse due to weak repulsive forces. Higher α (weaker attraction) requires shorter distances for amplification, but stronger repulsion increases the amplifiable range.

(e) Asymmetric elastic and magnetic forces in a symmetrical structure, and (f) its amplified motion as a function of distance when force anisotropy is controlled by γ, which is defined as the percentage difference between the two magnet-membrane pairs. The left pair consists of a membrane with modulus of (1-γ) E_0 and a magnet thickness of (*1*-γ) h_0, while the right pair uses a membrane with modulus of (1+γ) E_0 and a magnet with thickness of (1+γ) h_0. As γ increases, the stronger magnet is pulled more easily, enabling amplification over a larger range. However, larger γ causes weight imbalance, leading to uneven vibration motion between the magnets, even at the same distance from the electromagnet.

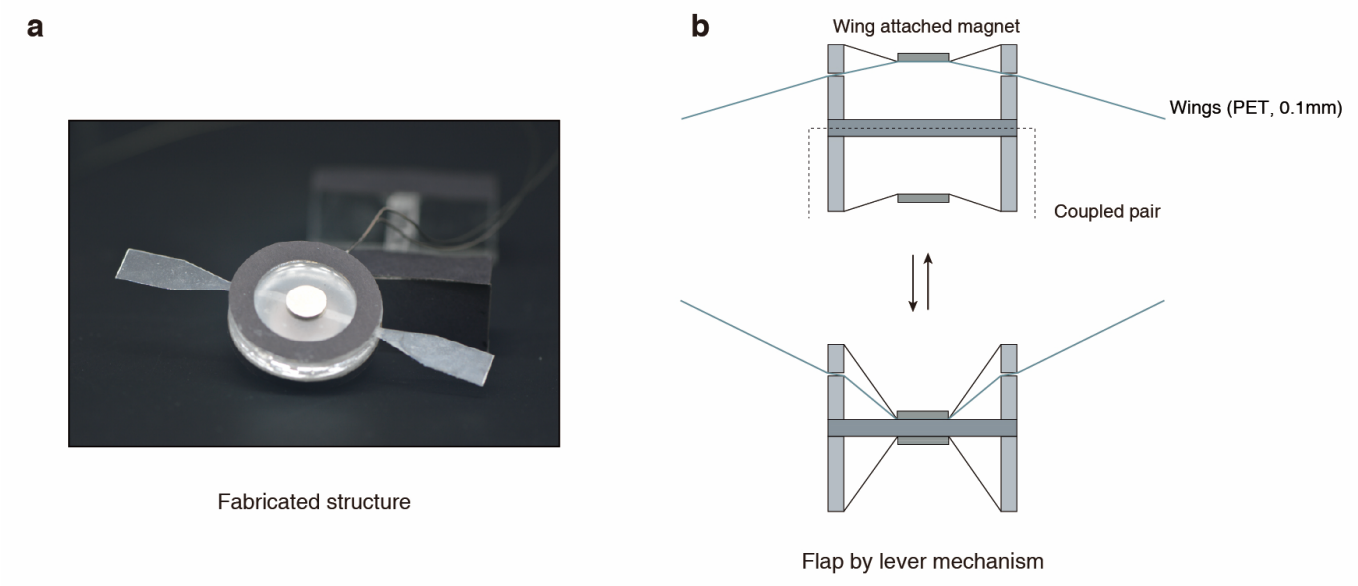

Supplementary Fig. 21. Structure and working mechanism for flapping wing demonstration.

(a) Photograph of C-EsMV system with PET film wings (0.1 mm) attached to a vibrating magnet. (b) The wing flaps through the lever mechanism as the magnet moves up and down.

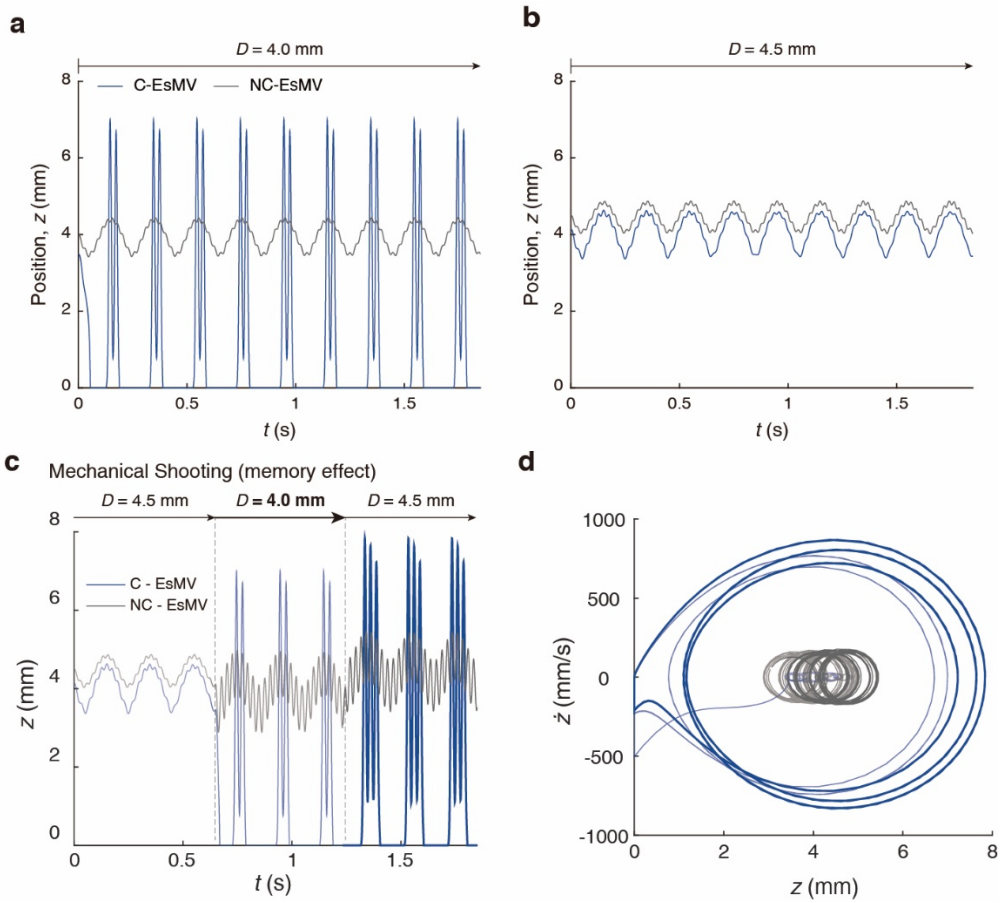

Supplementary Fig. 22. Numerical verification of mechanically triggered amplification.

Vibration motion of NC-EsMV and C-EsMV systems at an electromagnet-to-magnet distance of (a) $D = 4.0$ mm and (b) $D = 4.5$ mm, both under an input current of 2.0 A. (c) Analogous to the electrical shooting observed in Supplementary Fig. 13, mechanical triggering ($D = 4.5$ mm → 4.0 mm → 4.5 mm) also sustains amplified vibration in C-EsMV under constant input current, even after the trigger is removed. (d) Phase portraits of each system. The C-EsMV exhibits a larger-amplitude limit cycle (bold line) at the same input current and D, indicating greater vibration velocity and displacement compared with NC-EsMV.

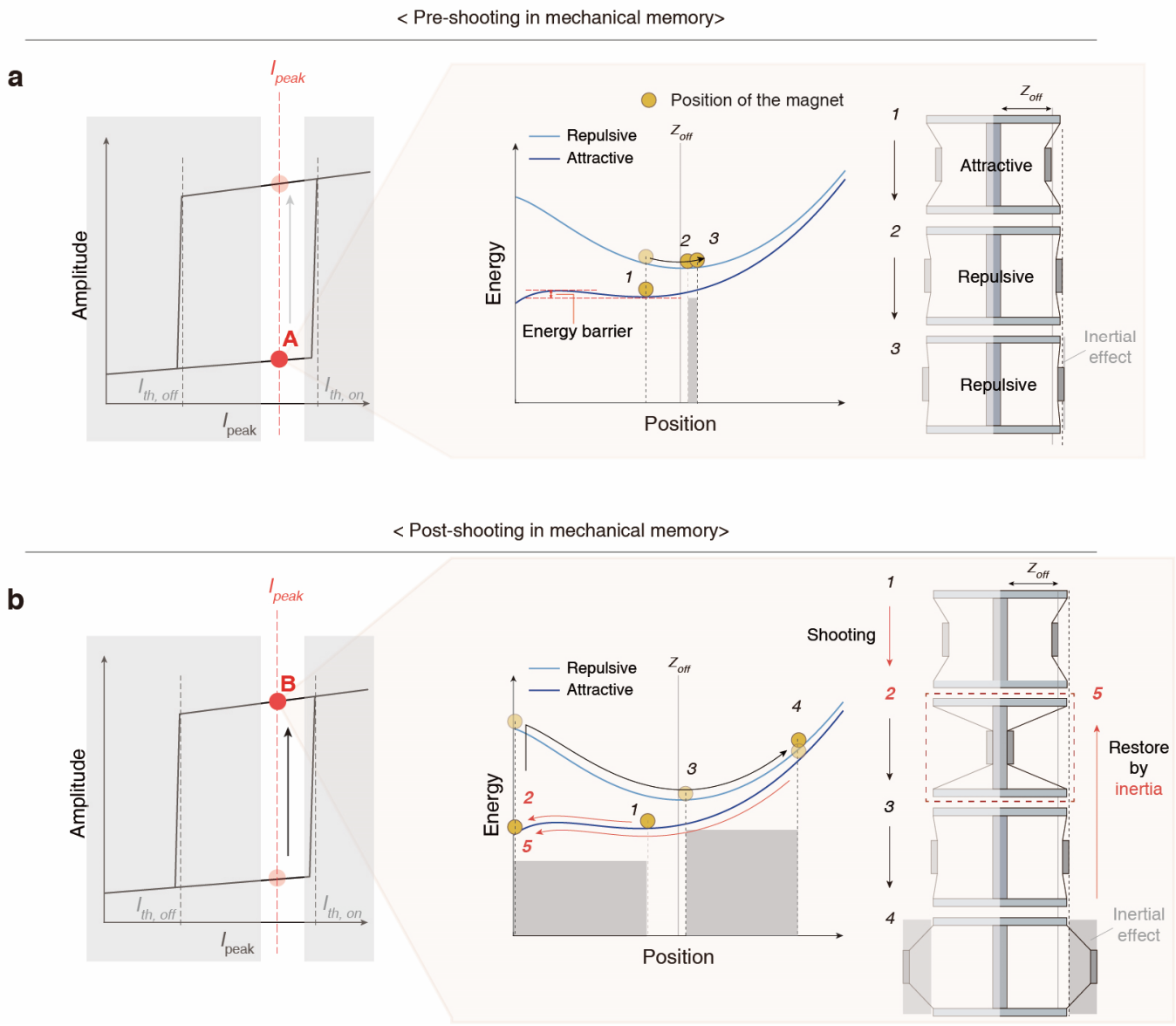

Supplementary Fig. 23. Mechanism of vibrational hysteretic behavior in mechanical memory.

Under identical input current I_{peak}, inertia allows two distinct vibration responses: (a) Pre-shooting (weakened state) and (b) post-shooting (amplified state). Without shooting, the magnet oscillates with small displacement near z_{off} (positions 1 – 3) unable to overcome the potential barrier imposed by magnetic attraction. As a result, the system remains in a low-amplitude vibration regime (Point A). By contrast, a brief perturbation (shooting)—which can be electrical, magnetic, or mechanical—pushes the magnet across the barrier to the bottom surface (z = 0, position "2"), storing additional elastic energy in the membrane. During the subsequent repulsive phase, this stored energy is released as a large overshoot ("3 → 4"), and the magnet returns with sufficient inertia to repeatedly cross the barrier ("4 → 1 → 5 (= 2)"). The residual kinetic energy from each cycle sustains these large-amplitude oscillations even after the external trigger is removed, corresponding to Point B on the amplitude–I_{peak} curve. If this residual energy is intentionally dissipated (see Supplementary Video 7), the system reverts to the weakened state.

Potential energy-position graphs are based on Supplementary Fig. 9e.

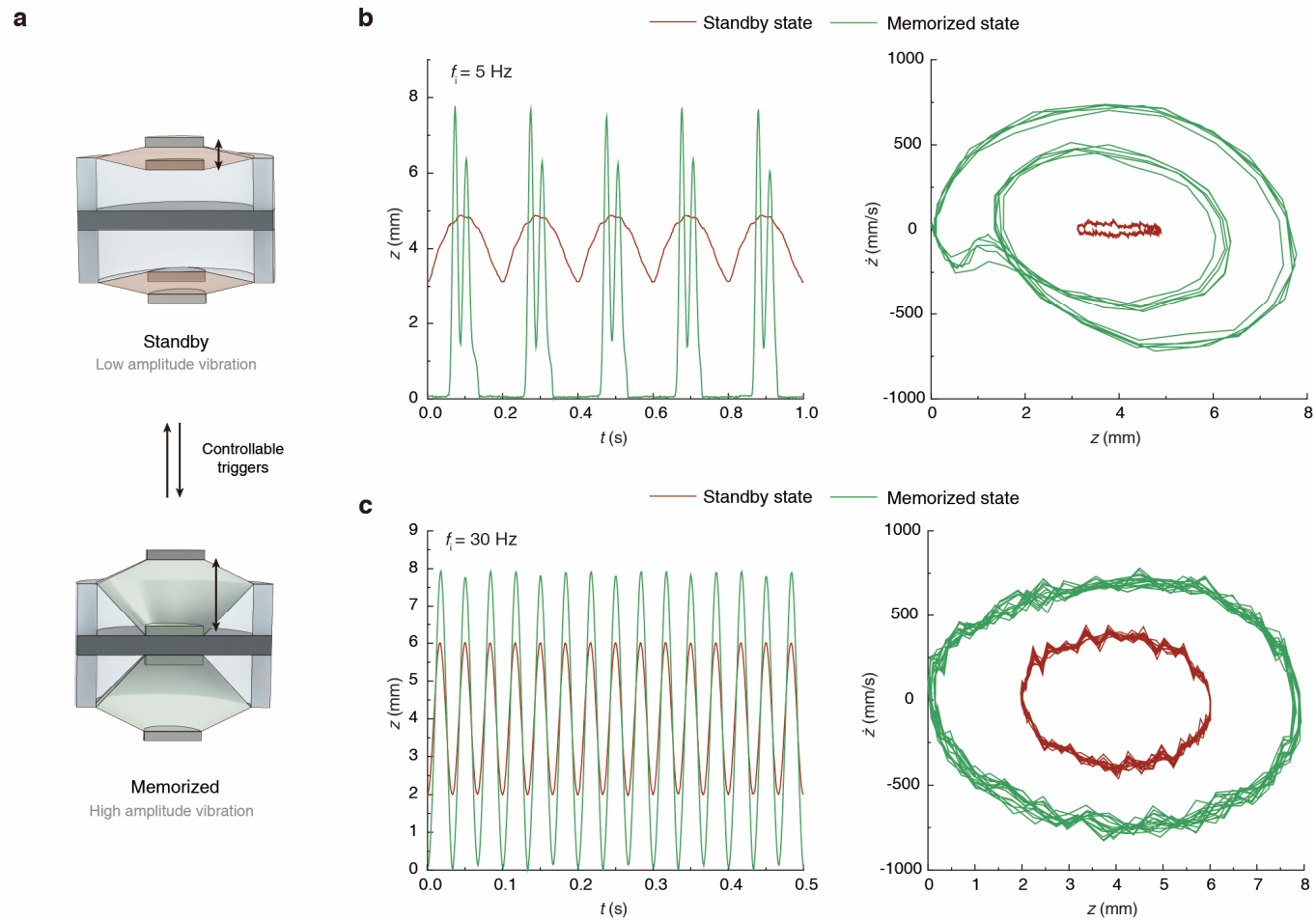

Supplementary Fig. 24. Experimental dynamic vibration response of the mechanical memory in standby and memorized states.

(a) Conceptual illustration of the mechanical memory. (b) Time-dependent vibration response and corresponding phase portrait at 5 Hz, comparing the standby (low-amplitude) and memorized (amplified) states. (c) Dynamic vibration response and phase portrait near resonance (30 Hz).

Supplementary Fig. 25. Experimental setup for mechanical memory and its operating modes.

(a) Basic unit cell of the mechanical memory system. (b) The unit cell is triggered using a push accessory at a speed of 500 mm/min, with approach and retract speeds indicated.

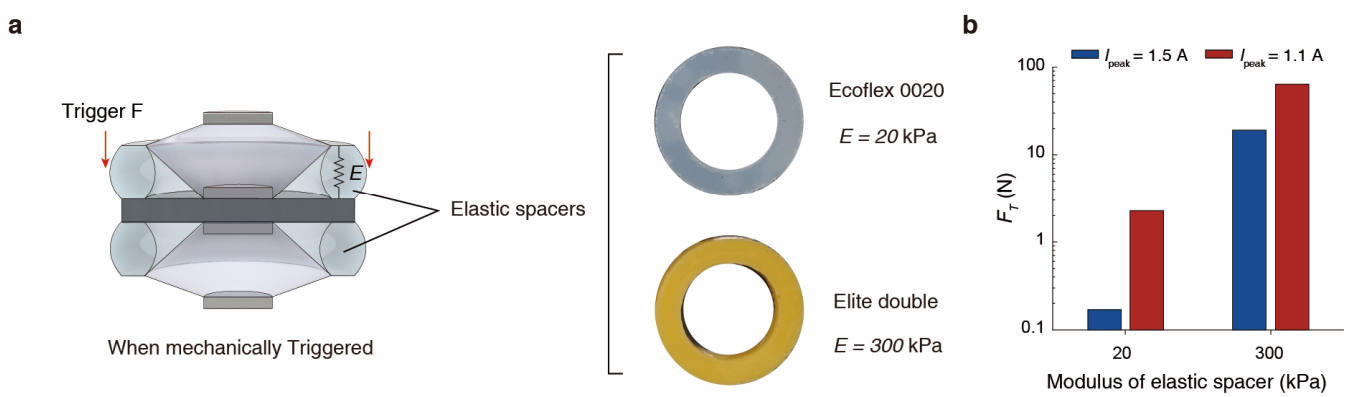

Supplementary Fig. 26. Trigger force characterization with elastic spacers of different elastic moduli.

(a) Schematic illustration of the elastic spacer setup, showing two spacers with different moduli, E = 20 kPa and E = 300 kPa. (b) Trigger force required for amplified vibration in each spacer. When the input current is close to the threshold ($I \approx I_{th}$, I_{peak} = 1.5 A), even small forces can surpass the threshold, resulting in low trigger force. As the current deviates from I_{th} (I_{peak} = 1.1 A), greater force is required to achieve amplification. Experiments were conducted under *R3* conditions, where amplification is sustained after the trigger in both cases.

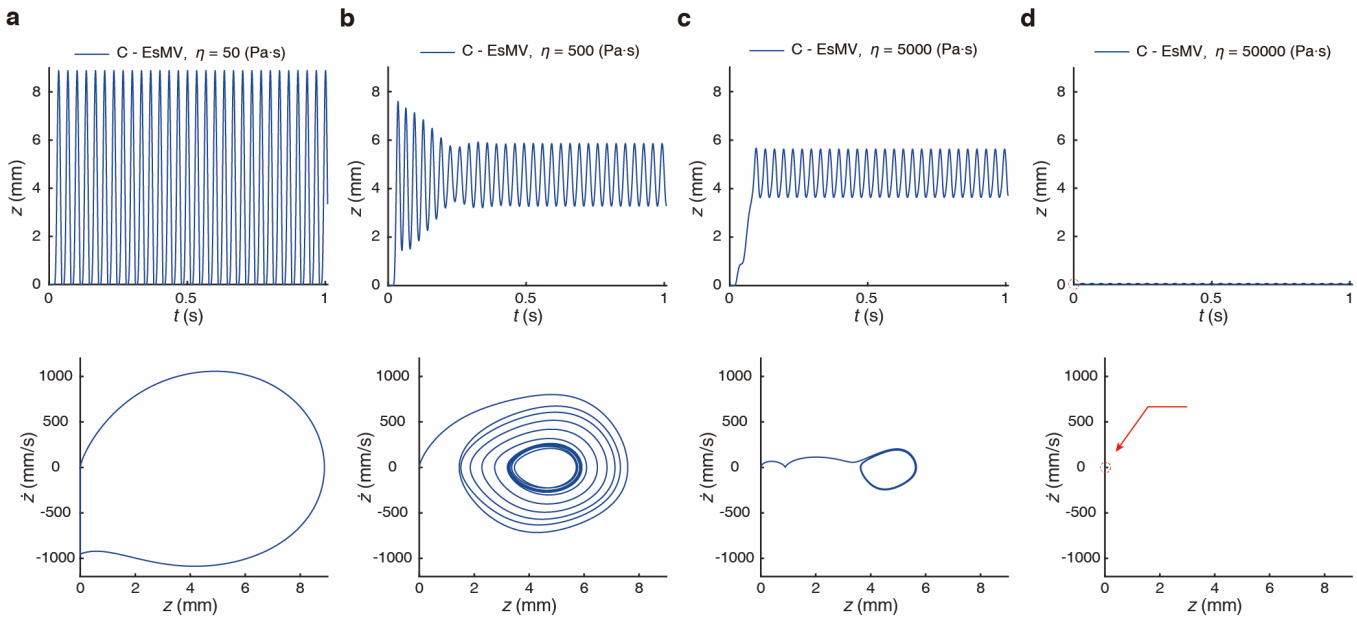

Supplementary Fig. 27. Effect of membrane damping on mechanical memory. (a) η = 50 (b) η = 500 (c) η = 5000 (d) η = 50000 Pa·s.

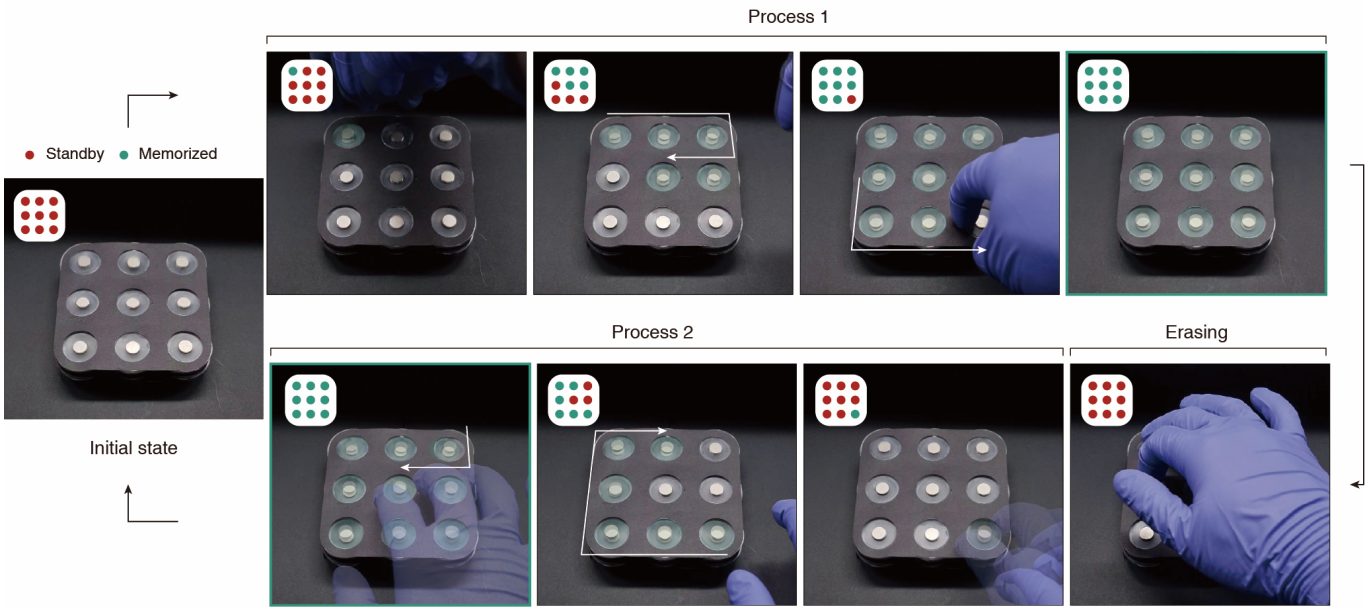

Supplementary Fig. 28. The entire process of non-volatile mechanical memorization.

When a trigger displacement is applied by pressing the spacer from the standby state, the system traces and stores the mechanical trigger. By placing a hand near the vibrating magnet, the energy is dissipated, erasing the memory. The system can then re-memorize the trigger, regardless of the previous path.

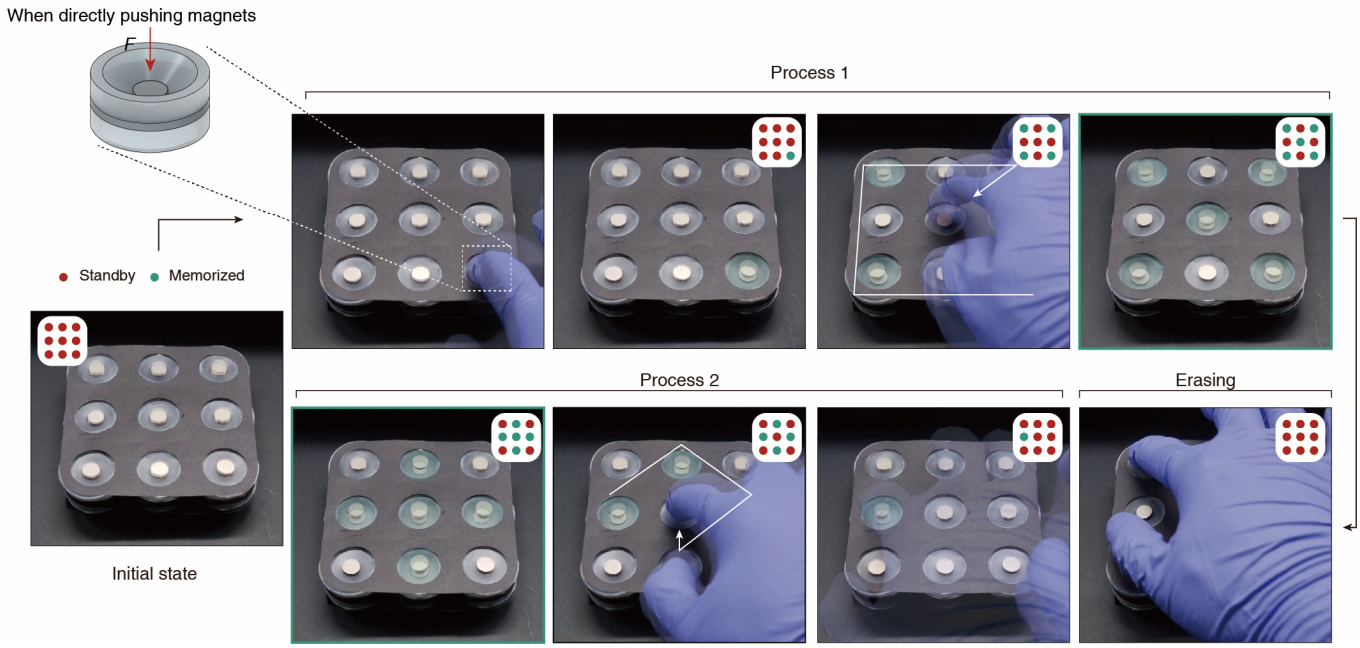

Supplementary Fig. 29. Non-volatile mechanical memorization by directly pressing the magnet.

Pressing the magnet attached to the membrane, instead of the spacer, raises the maximum elastic potential energy. This creates a similar effect to mechanical shooting, enabling amplified vibrations and non-volatile mechanical memorization.

Supplementary references.

1. Ogden, R. W. Non-linear elastic deformations. *Courier Corporation* (1997).
2. Thomson, W. IV. On the elasticity and viscosity of metals. *Proc. R. Soc. Lond*. **14**, 289-297 (1865).
3. Sosa, V. Alternative method to calculate the magnetic field of permanent magnets with azimuthal symmetry. *Revista mexicana de física E*, **59**, 8-17 (2013).
4. Pollack, G. L. & Stump, D. R. *Electromagnetism*, (Addison-Wesley, Boston, 2001).